MICROCOPY RESOLUTION TEST CHART
NATIONAL BUREAU OF STANDARDS-1963-A

AD-A182 489

REPORT DOCUMENTATION PAGE

Form Approved
OMB No. 0704-0188

1a. REPORT SECURITY CLASSIFICATION	1b. RESTRICTIVE MARKINGS
UNCLASSIFIED	N/A

2a. SECURITY CLASSIFICATION AUTHORITY	3. DISTRIBUTION/AVAILABILITY OF REPORT
N/A	Approved for public release; distribution
2b. DECLASSIFICATION/DOWNGRADING SCHEDULE	unlimited.
N/A	

4. PERFORMING ORGANIZATION REPORT NUMBER(S)	5. MONITORING ORGANIZATION REPORT NUMBER(S)
UTEC MD-86-064	RADC-TR-87-23

6a. NAME OF PERFORMING ORGANIZATION	6b. OFFICE SYMBOL (If applicable)	7a. NAME OF MONITORING ORGANIZATION
University of Utah		Rome Air Development Center (OCTP)

6c. ADDRESS (City, State, and ZIP Code)	7b. ADDRESS (City, State, and ZIP Code)
Department of Electrical Engineering Salt Lake City UT 84112	Griffiss AFB NY 13441-5700

8a. NAME OF FUNDING/SPONSORING ORGANIZATION	8b. OFFICE SYMBOL (If applicable)	9. PROCUREMENT INSTRUMENT IDENTIFICATION NUMBER
AFOSR	NE	F30602-82-C-0161

8c. ADDRESS (City, State, and ZIP Code)	10. SOURCE OF FUNDING NUMBERS			
Bolling AFB Wash DC 20332	PROGRAM ELEMENT NO.	PROJECT NO.	TASK NO.	WORK UNIT ACCESSION NO.
	61102F	2305	J9	16

11. TITLE (Include Security Classification)
DEVELOPMENT OF A DYNAMIC SECONDARY EMISSION MODEL FOR USE IN MDC SIMULATIONS

12. PERSONAL AUTHOR(S)
David J. Ferretti

13a. TYPE OF REPORT	13b. TIME COVERED	14. DATE OF REPORT (Year, Month, Day)	15. PAGE COUNT
Final	FROM Sep 82 TO Oct 86	April 1987	

16. SUPPLEMENTARY NOTATION
Research accomplished in conjunction with Air Force Thermionics Engineering Research (AFTER) Program (AFTER-19)

17.	COSATI CODES		18. SUBJECT TERMS (Continue on reverse if necessary and identify by block number)
FIELD	GROUP	SUB-GROUP	Traveling Wave Tubes Computer Modeling
09	03		Multiple Depressed Collectors Secondary Emission

19. ABSTRACT (Continue on reverse if necessary and identify by block number)

There is a strong need in the tube industry to develop good simulational design tools. An area where this is most evident is multistage depressed collector simulation.

This thesis is an attempt to improve this simulation through the development and inclusion of a physically accurate secondary emission model. The model developed in this report includes provisions for various energy primary electrons, as well as various angles of primary impact. The model developed in this manner was then tested by making calculations on an existing traveling-wave tube.

20. DISTRIBUTION/AVAILABILITY OF ABSTRACT	21. ABSTRACT SECURITY CLASSIFICATION
☒ UNCLASSIFIED/UNLIMITED ☐ SAME AS RPT. ☐ DTIC USERS	UNCLASSIFIED
22a. NAME OF RESPONSIBLE INDIVIDUAL	22b. TELEPHONE (Include Area Code)	22c. OFFICE SYMBOL
Andrew E. Chrostowski, Capt, USAF	(315) 330-4381	RADC (OCTP)

DD Form 1473, JUN 86   Previous editions are obsolete.

ACKNOWLEDGMENTS

Accession For		
NTIS CRA&I	⊠	
DTIC TAB	☐	
Unannounced	☐	
Justification		
By		
Distribution/		
Availability Codes		
Dist	Avail and/or Special	
A-1		

TABLE OF CONTENTS

LIST OF ILLUSTRATIONS AND TABLES

I. INTRODUCTION

Increased demand for higher power, light weight, microwave power tubes has promoted much interest in the design and development of more efficient electron beam collectors. To this end, several major areas of study have been conducted in greater detail. Included among these are conditioning and/or refocusing of the spent electron beam prior to injection into the collector, multistage depressed collectors (MDC), and low yield collector materials. As a result of this research, it is presently possible to achieve collector efficiencies upwards of 80 percent, resulting in a substantial increase in overall tube efficiency.

In addition to the areas mentioned above, which affect changes in collector performance via changes in the basic collector design, an extensive effort has been made to develop an accurate simulation model of a circularly symmetric traveling-wave tube (TWT) collector. One model which has been used extensively, with generally favorable results, was developed by J. A. Dayton, Jr., H. G. Kosmahl, P. Ramins, and N. Stankiewicz at the National Aeronautics and Space Administration's (NASA) Lewis Research Center (LRC). Several papers[1,2,3,4] have been published verifying the performance of this model for a number of different tube types with MDCs optimized for a variety of operating conditions. In predicting collector efficiency, the deviation from actual results was less than 10 percent for all cases reported. In fact, the majority of the computational predictions were accurate to within 5 percent of the actual value. On the other hand, predictions of

collector electrode current distributions were often in much larger disagreement with experimentally obtained results.

One aspect of collector operation which received only an elementary treatment in the LRC model is that of secondary electronic emission. The major objective of this thesis is to develop a secondary emission model consistent with the physical emission characteristics of the most commonly used collector materials; an additional objective being relatively easy computer implementation.

The format used in the remainder of this text will be a rather extensive outline and discussion of the most pronounced and relevant emission properties of metals. This will be followed by the development of the emission model. Included in this section is the method of quantization of the yields, as well as the methods used in the extension of previously reported data to the entire domain of primary energy and incidence. A brief discussion of the method used in modeling the TWT from RF input to beam collection will follow. And, finally, the model's performance will be verified and recommendations for future areas of improvement will be made.

II. SECONDARY EMISSION OVERVIEW

A. Introduction to the Overview

Before getting into the details of the actual emission model, it is instructive to take a closer look at some relevant aspects of secondary emission. Experimental research into various modes of secondary electron production has been extensive; however, the present interest in electron collection does not warrant a general review of this broad subject. Since many commonly used collector materials are polycrystalline in nature, empirical results for polycrystalline metal surfaces, bombarded by electrons, are most applicable. Thus, it is this empirical data for which the following discussion of secondary emission holds.

The phenomenon of secondary emission was first observed by Austin and Starke when they noticed that, given proper conditions, more electrons were emitted from a sample of metal than impinged upon it. This observation suggested that some mechanism existed which promoted electron liberation from the sample. Subsequent experiments have played a major role in the development of several basic concepts presently used in the applications of secondary emission.

B. Secondary Electron Energy Classification

One of the first observations made was that emitted electrons may be subgrouped into one of two classes: true or slow secondaries, and fast or elastically scattered secondaries, with each group exhibiting its own unique emission properties. Figure 1 is a typical curve of yield versus secondary electron (SE) energy for a metal being bombarded
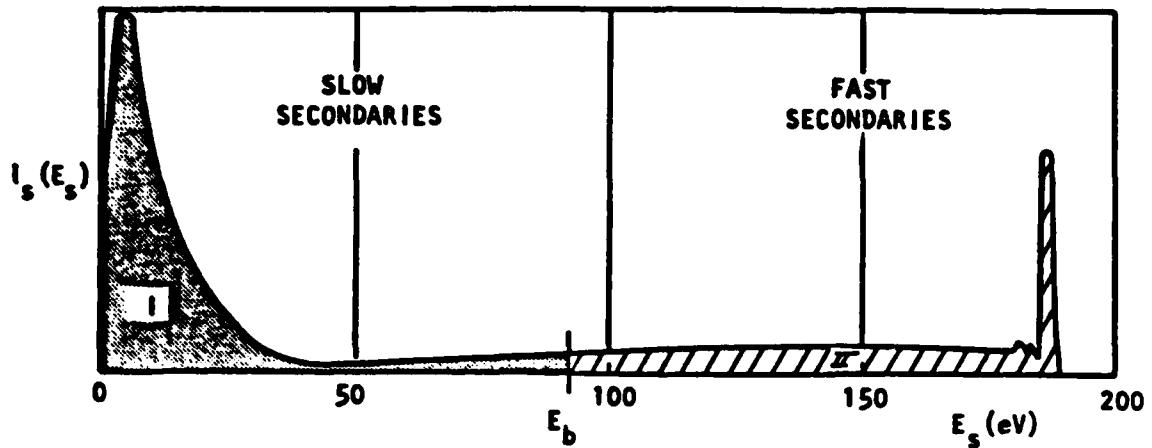
Fig. 1. General secondary yield for a metal
as a function of secondary energy.

by a normally incident stream of primary electrons (PEs) with energy
E_p. Although there is actually no clear cut SE energy which separates
the elastically from inelastically scattered secondaries, region I is
generally assumed to be entirely composed of slow secondaries. Simi-
larly, region II is assumed to be entirely composed of elastically
scattered secondaries.

The choice of the boundary used to separate the two regions is
somewhat arbitrary. For E_p greater than 100 eV, some researchers[5] sug-
gest using a value of E_b (Fig. 1) approximately equal to 1/2 E_p; how-
ever, a SE energy of 50 eV is more commonly used as the transition
point.[6,7,8,9] Therefore, unless otherwise stated, it is assumed that
any data discussed in this thesis were taken using the value of 50 eV as
the boundary.

- 4 -

C. Slow Secondary Emission Characteristics

Although treated as one group, slow secondaries may be further decomposed into two distinct groups of electrons: true secondaries and inelastically reflected primaries. As is apparent by the component names, the most obvious distinction between the two is their origins. True secondaries are those electrons which are actually liberated by the solid being bombarded, whereas inelastically reflected primaries are primary electrons which have undergone one or more inelastic collisions and then been reflected into the sample's surroundings. It is interesting to note that the true secondaries, hencefore referred to interchangeably as slow secondaries, are responsible for any yields greater than unity, since this is the only class of secondaries not composed of scattered primaries.

Many experiments have been performed by Jonker[10] in an attempt to determine the angular distributions of three discrete energy classes of secondaries emitted by polycrystalline nickel. However, due to the range of primary energies tested, a fixed threshold of 50 eV proved to be inadequate in distinguishing the slow and fast secondaries. Table 1 lists the energy groupings used by Jonker for what he terms the slow, moderate, and fast secondaries, presented as a function of E_p. Results of these experiments indicate that the slow and moderate secondaries exhibit similar distribution characteristics. Thus, it is assumed that a combination of the two energy classes produces a total distribution which may be approximated by the slow secondary distribution.

- 5 -

Table 1. Energy groupings of the slow, moderate,
and fast secondaries used by Jonker[10] in
his emission distribution measurements.

Primary Electrons: Bombardment Voltage	Slow Secondary Electrons	Secondary Electrons with Moderate Velocity	Rapid Reflected Electrons
25 volts	1 to 6 volts	10 to 15 volts	20 to 25 volts
100 volts	5 to 15 volts	45 to 55 volts	80 to 100 volts
450 volts	0 to 10 volts	*	360 to 450 volts
* Current density was below observation limit			

For normally incident primaries, with energies on the order of 20
eV, Jonker experimentally observed a slow secondary emission distribu-
tion very closely resembling the cosinusoidal distribution shown in Fig.
2. Contrarily, other combinations of incident angle and PE energy were
found to produce results which deviated noticeably from this idealized
distribution. In commenting on his results, Jonker suggested several
plausible explanations for this, but since it is the observable changes
in the distribution and not the mechanisms giving rise to those that are
of the most interest here, these explanations will not be given and the
interested reader is referred to reference 7. Instead, observations on
the macroscopic distribution changes with PE energy and incident angle
will be discussed.
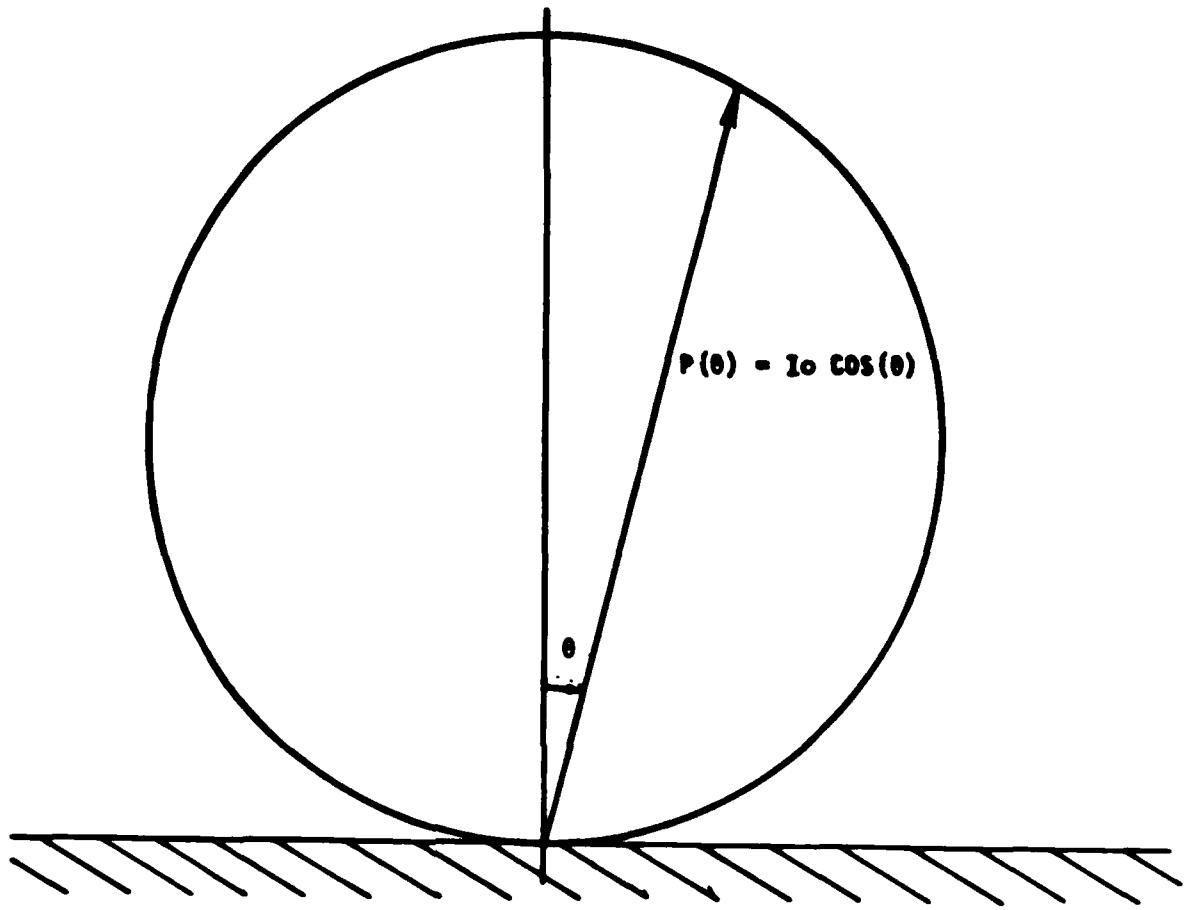
Fig. 2. An ideal cosinusoidal emission distribution function P(θ).

From Figs. 3a and 3b, it is evident that a slightly increased emission, biased in a direction approximately antiparallel to that of the PE velocity vector, develops as the incident angle is rotated through 45 degrees. The magnitude of emission increase seems to be more pronounced at higher incident energies. But, until more detailed distribution measurements are available, no conclusions may be drawn as to
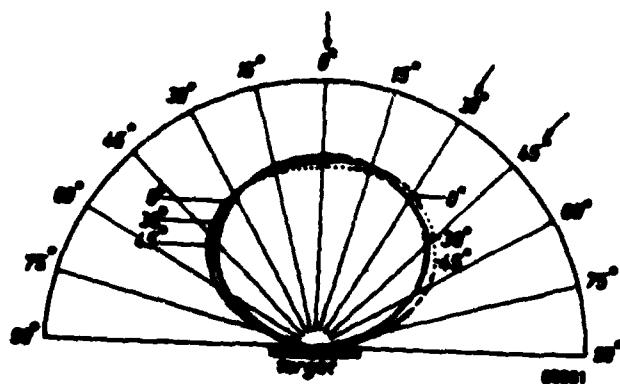
(a)
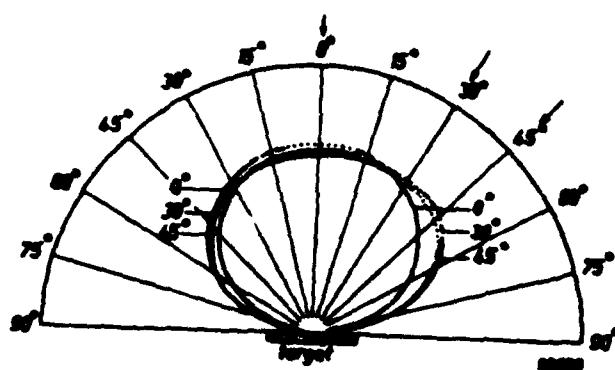
(b)

Fig. 3. Jonker's[10] measured angular distributions for slow
secondaries emitted by polycrystalline nickel.
(a) E_p = 100 eV, distributions for several
angles of incidence.
(b) E_p = 450 eV, distributions for several
angles of incidence.

- 8 -

whether or not additional increases in PE energy would distort the distribution even further. It may be inferred, however, that deviations from the cosinusoidal distribution, resulting from excitation at oblique incidence, are not excessive.

Figures 4a, 4b, and 4c provide useful insight into the behavior of the slow secondary emission distribution for changes in primary energy with the angle of incidence being held constant. Assuming that the best approximation to a perfect cosinusoidal distribution in each figure is the 25 eV curve, a slight flattening of the circularly symmetrical distribution occurs with initial increase in primary energy. Additional increases in energy result in a slight elongation of the initial distribution for normal incidence, indicating a slightly preferred direction of emission. However, for the case of oblique incidence, an additional flattening of the distribution is observed which indicates a slight increase in the solid angle of emission relative to the surface normal.

From Figs. 4a and 4c, apparently none of the energy related distributions deviate from the others by an appreciable amount. Similarly, the distributions for the 25 eV and the 100 eV curves shown in Fig. 4b also track each other reasonably well. Although a larger deviation from curves of similar angle incidence is exhibited by the 45 eV distribution of Fig. 4b, the resulting deviation, while significant, is still not a predominant feature. From these observations, it is apparent that generally the emission distributions for variable energy tend to track each other at normal incidence better than the distributions shown in Fig. 3 for variable angle of incidence. Thus, it may be concluded that the slow secondary emission distribution is slightly more dependent on

- 9 -
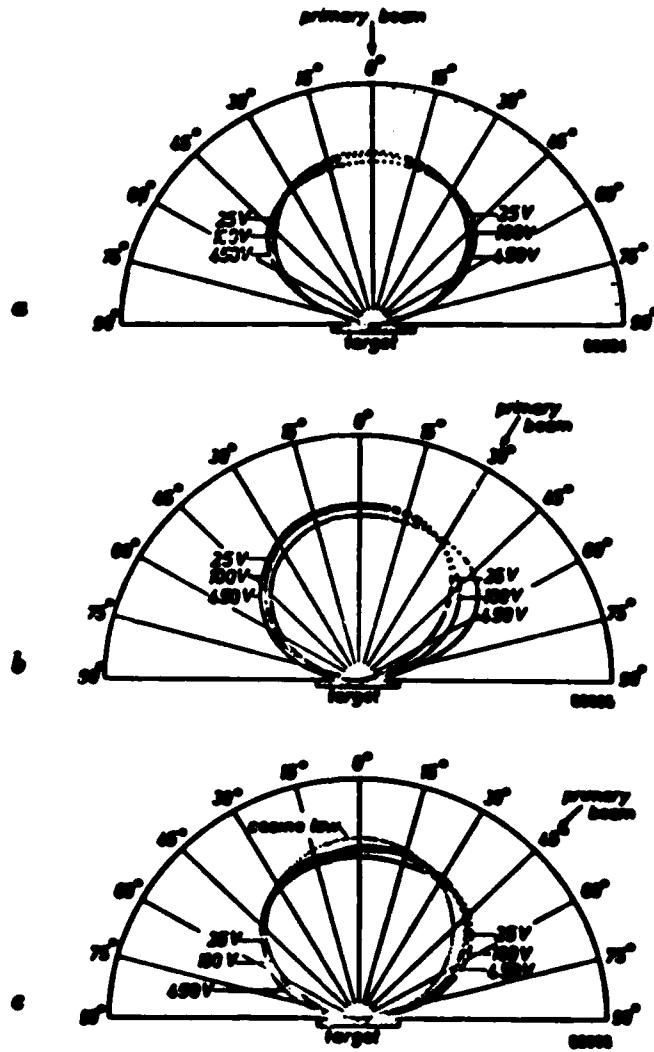
Fig. 4. Jonker's[10] measured angular distributions for slow
secondaries emitted by polycrystalline nickel.
(a) $\theta_i = 0°$, distributions for several values of E_p.
(b) $\theta_i = 30°$, distributions for several values of E_p.
(c) $\theta_i = 45°$, distributions for several values of E_p.

the angle of incidence than on primary energy for fine grain applications.

Overall, the results published by Jonker seem to indicate that for most practical applications, the slow secondary emission function to a first order approximation is independent of incident angle, as well as primary energy. Furthermore, this basic distribution may be adequately approximated as a cosinusoidal distribution. Although true secondaries comprise a major part of the total yield, the remaining yield component's distribution characteristics need also be examined. In fact, due to the anticipated effects of space-charge suppression on true secondary yield, it is this class of secondaries which is expected to play a more significant role in the actual electrode current distributions.

D. Fast Secondary Emission Characteristics

The second group of electrons comprising the remaining portion of the total emission is referred to collectively as fast, or elastically, scattered secondaries. This group of secondaries is mainly composed of primary electrons which have undergone one or more elastic collisions within the sample and then been deflected out. Although only a small fraction of the total, the remainder of the elastically scattered electrons is comprised of lattice electrons which have undergone an elastic collision with a PE and then been liberated from the sample through electron substitution or a similar process.

As in the case of slow secondaries, any differences in emission characteristics resulting from the secondaries origin are irrelevant, since our emicsion model will treat all secondaries emitted in the fast

- 11 -

energy class collectively. Again, the measurements of fast secondary distributions used for illustration were taken by Jonker. In his report on the emission distributions of polycrystalline nickel,[10] several measured fast secondary distributions are presented for a variety of PE incident angles and energies. For convenience, these results are repeated here in Figs. 5 and 6, with the energy range used for the fast secondaries, as before, being defined in Table 1.

From Fig. 5, it is evident that there are a number of characteristics common to some of these fast secondary distributions which merit noting. Probably the most obvious is the bidirectional nature of the distributions shown in Fig. 5 for oblique incidence. For each of these distributions, two distinct lobes are evident, indicating the existence of two local emission maxima. Surprisingly, emission for the larger of the two lobes occurs in a backward direction with respect to the component of the PE velocity parallel to the surface, while emission for the smaller lobe occurs in the forward direction. Thus, simple application of Snell's law would be inappropriate.

Another very noticeable difference between the slow and fast distributions measured by Jonker is the angular width of the emission lobes. As seen in Figs. 5 and 6, both of the emission lobes for each of the fast secondary distributions are generally narrower than those of the slow secondary distributions shown in Figs. 3 and 4. This characteristic indicates that the fast secondaries will be emitted over a smaller solid angle so that, statistically, a more directional emission will result.
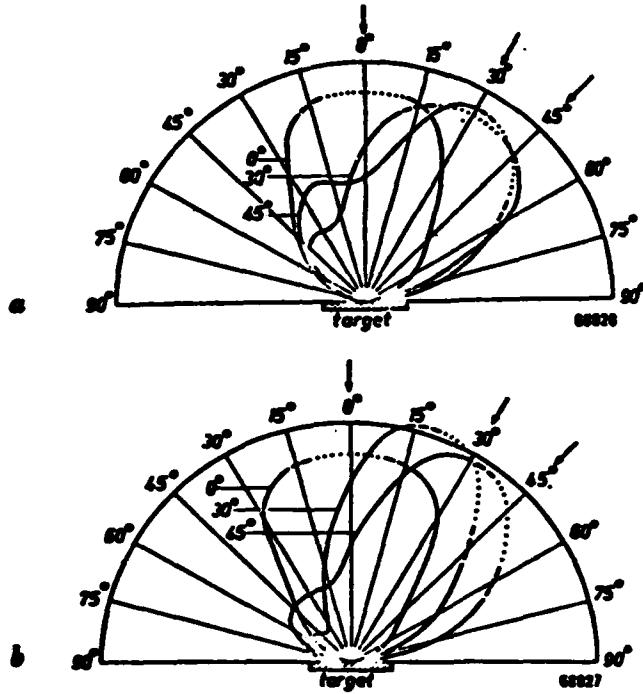
Fig. 5. Jonker's[10] measured angular distributions for fast
secondaries emitted by polycrystalline nickel.
(a) E_p = 100 eV, distributions for several
angles of incidence.
(b) E_p = 450 eV, distributions for several
angles of incidence.
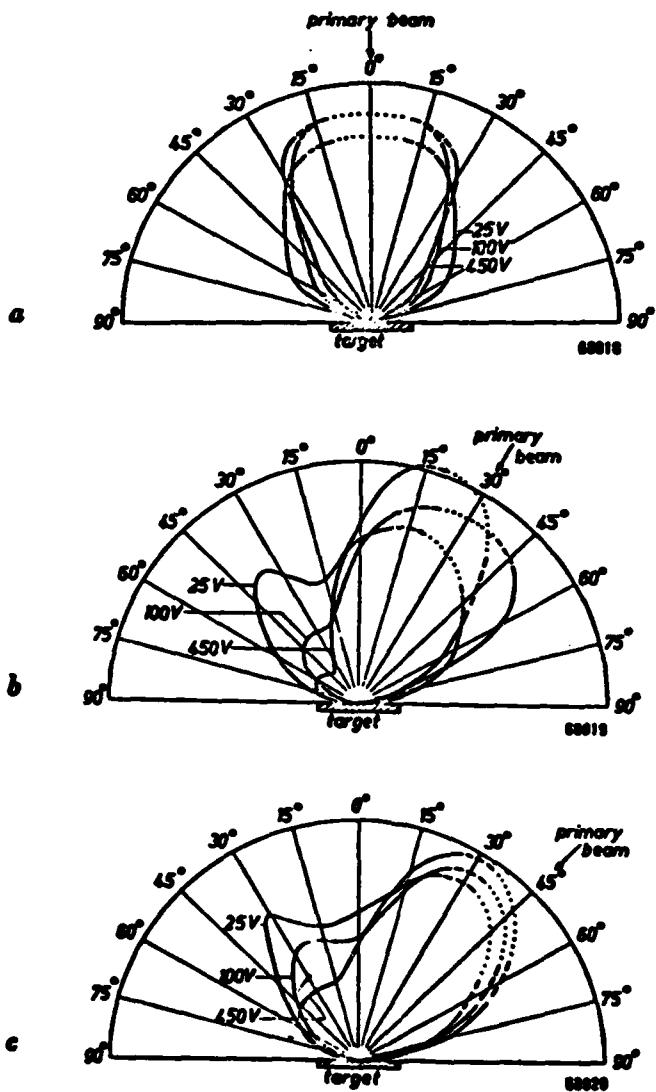
Fig. 6. Jonker's[10] measured emission distributions for fast
secondaries emitted by polycrystalline nickel.
(a) $\theta_i = 0°$, distributions for several values of E_p.
(b) $\theta_i = 30°$, distributions for several values of E_p.
(c) $\theta_i = 45°$, distributions for several values of E_p.

- 14 -

From Fig. 6, it can be seen that with increasing primary energy, the magnitude of the secondary lobe decreases and that of the primary lobe increases. Additionally, a decrease in primary lobe width is also observed for higher energies. The implication of these last two trends with energy is that for a very high energy PE, virtually all elastic emission will take place in a single reverse direction. It seems feasible that this characteristic behavior may be exploited in future collector design, especially those in which secondary suppression, not efficiency, is the prime concern.

E. Secondary Electron Component Yield Coefficients

As mentioned before, several other emission characteristics have been first observed through experimental investigation. One of these characteristics from which a complete set of yield data may be obtained for a particular material is the variation in the secondary emission energy distribution with PE energy and incident angle.

An indication of the existence of the dependency on primary energy may be seen in Fig. 7, which shows the SE energy distributions of molybdenum for a number of PE energies impinging at normal incidence. However, the utility of the data for molybdenum is limited because the corresponding data providing the dependencies upon incident angle have not been reported.

While the above data for molybdenum may not be useful in itself, with a slight explanation it does imply that if the secondary energy distribution varies with PE energy and incident angle, the component yields will also. The integration of the SE energy distribution over

- 15 -
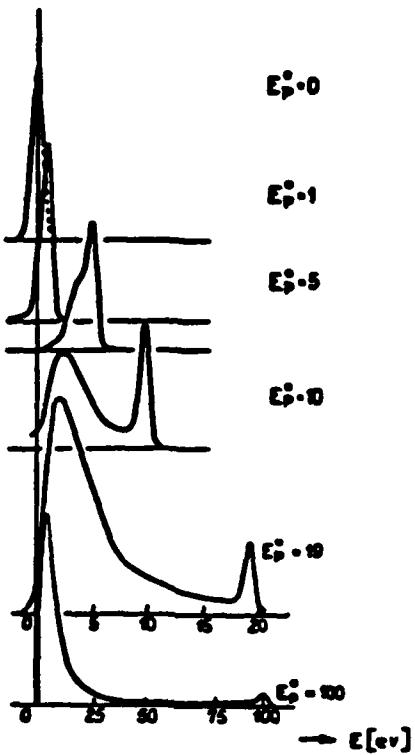
Fig. 7. Secondary electron energy distribution for a Mo target for several primary energies as taken from Hachenberg and Brauer.[7] This figure was originally presented by G. A. Harrower.[11]

the entire SE energy spectrum gives the total yield, σ_t, for the given primary beam energy and incident angle specific to that spectrum. Thus,

$$\sigma_t\left(E_p, \theta_i\right) = \int_o^\infty i_s\left(E_s\right) dE_s \qquad (1)$$

Similarly, since the two regions of Fig. 1 are the commonly accepted domains of the slow and fast secondaries, separate integrations performed over the defining energy ranges will return the total yield of slow and fast secondaries. Thus, letting σ_s be the total yield of slow secondaries and σ_f be the total yield of fast secondaries, the relations

- 16 -

$$\sigma_s(E_p, \theta_1) = \int_{E_b}^{\infty} i_s(E_s) \, dE_s \qquad (2)$$

and

$$\sigma_f(E_p, \theta_1) = \int_{E_b}^{\infty} i_s(E_s) \, dE_s \qquad (3)$$

follow. As is apparent from defining Eqs. 1 through 3, the sum of the slow and fast secondary yield is the total yield. Thus, the knowledge of how any two of the above yields vary, with PE energy and incidence for a given material, is sufficient in characterizing the secondary emission yield properties for that material.

Using a spherical retarding-field analyzer, Koshikawa and Shimizu[8] made extensive measurements of SE yield coefficients for smooth polycrystalline copper. In principle, the analyzer was designed to evaluate expressions 1 and 3. However, due to the assumed monoenergetic division of the slow and fast secondary domains, slight deviations from the physical yield coefficients are probable, although unimportant for our purposes.

The results obtained from these experiments for the yield and backscattering coefficients are shown here in Figs. 8 and 9, respectively. It is important to reiterate that the data presented in these figures provide complete component yield information for polycrystalline copper at each of the discrete PE energy-incident angle pairs used in the measurements.

- 17 -
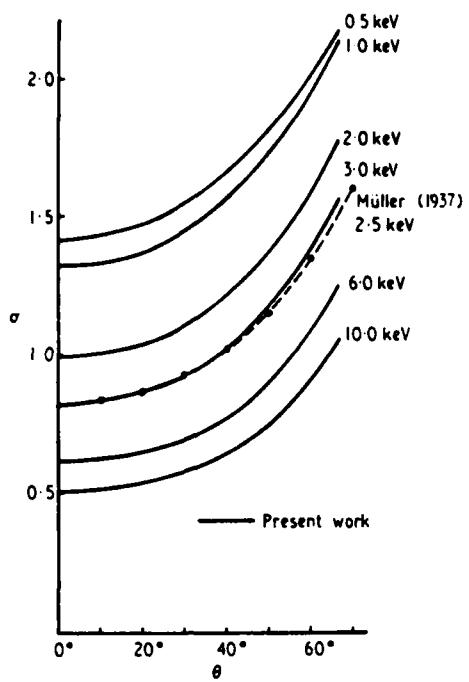
Fig. 8. Total secondary electron yield versus angle of
incidence for a number of primary electron
energies using a polycrystalline copper target.[8]
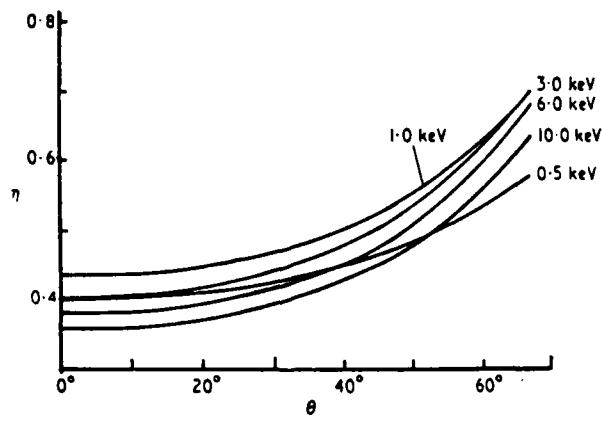
Fig. 9. Backscattering coefficient versus angle of
incidence for a number of primary electron
energies using a polycrystalline copper target.[8]

- 18 -

F. Yield Variations with PE Initial Conditions

There are several notable features of the total yield curves shown in Fig. 8 which should be discussed. The first is that for each of the primary energy curves shown, the minimum emission occurs for normal incidence, with a local maximum occurring at the largest measured angle. Work done by Muller[12] indicates that the yield would continue to rise for even larger angles of incidence, with the local maximum over this range expected for grazing incidence. From these results, it appears that the total yield, at least for polycrystalline copper, is a monotonically increasing function with increasing incident angle.

Another interesting feature of these yield curves is the approximately uniform spacing between curves of different primary energy. The most obvious implication of this is that if the yield at normal incidence is subtracted off, then the shape of the resulting yield curves with incident angle will all be approximately the same. Thus, it seems that this feature may be utilized in constructing a similar family of curves for other materials, once the variation in yield with PE energy and the general shape of the yield curve versus incident angle are known for these materials.

Additional research[13,14] has also shown that the extent of yield variation over all angles of incidence is very strongly affected by the surface texture, since no true normal to the surface exists for rough surfaces. Thus, by suitable texturing of the surface, it is possible to reduce significantly the yield dependence upon incident angle.

Similar tendencies to those of total yields are exhibited by each of the curves shown in Fig. 9 for the backscattering coefficients. As could be expected, the backscattering coefficient is also a monotonically increasing function of the incident angle. However, a major difference between the two families of curves is evident in the extent of functional variation with incident angle.

For illustrational purposes, it is convenient to define some figure of merit for the total functional variation with angle. Defining a quantity called the maximum percentage increase (MPI) as

$$MPI = \frac{\text{Functional value at the maximum angle}}{\text{Functional value at normal incidence}} \qquad (4)$$

it can be seen from Table 2 that the MPI of the total yield is a monotonically increasing function of energy, while that for the backscattering coefficient appears to reach a maximum somewhere between 3 and 10 keV. As well as the behavioral differences in these curves, it is evident from Table 2 that for all cases calculated, the MPI of the total yield is greater than that for the corresponding MPI of the backscattering coefficient. This last observation leads to several other interesting trends in yield composition.

Table 2. MPI figures for component yields.

	0.5 keV	1.0 keV	2.0 keV	3.0 keV	6.0 keV	10.0 keV
Total yield						
High	2.16	2.12	1.76	1.56	1.25	1.05
Low	1.41	1.32	0.991	0.820	0.621	0.505
Percent increase	153	161	178	190	201	209
Backscattered						
High	0.577	0.698		0.698	0.678	0.633
Low	0.401	0.436		0.402	0.380	0.360
Percent increase	144	160		174	178	176
Percent yield at normal incidence of slow secondaries	72	67		51	39	29

Since it appears that the total yield is greater than that for fast secondary yield, it seems intuitively obvious that the corresponding MPI of the slow secondary yield should also exceed that of fast secondaries. A formal proof that this is indeed true is presented in Appendix B. By itself, this observation may be misleading, since a larger MPI does not necessarily imply a larger gain in the number of emitted secondaries. However, for the energy range in which more than 50 percent of the total yield at normal incidence is composed of slow secondaries, changes in the absolute yield of slow secondaries are also larger than those of the fast secondaries. From Figure 10, it can be seen that for polycrystalline copper, this energy range is approximately 0 keV to 3 keV.

% CHANGE

300

200

100

1.0 2.0 3.0 4.0 5.0 6.0 7.0 8.0 9.0 10.0

E_p(keV)
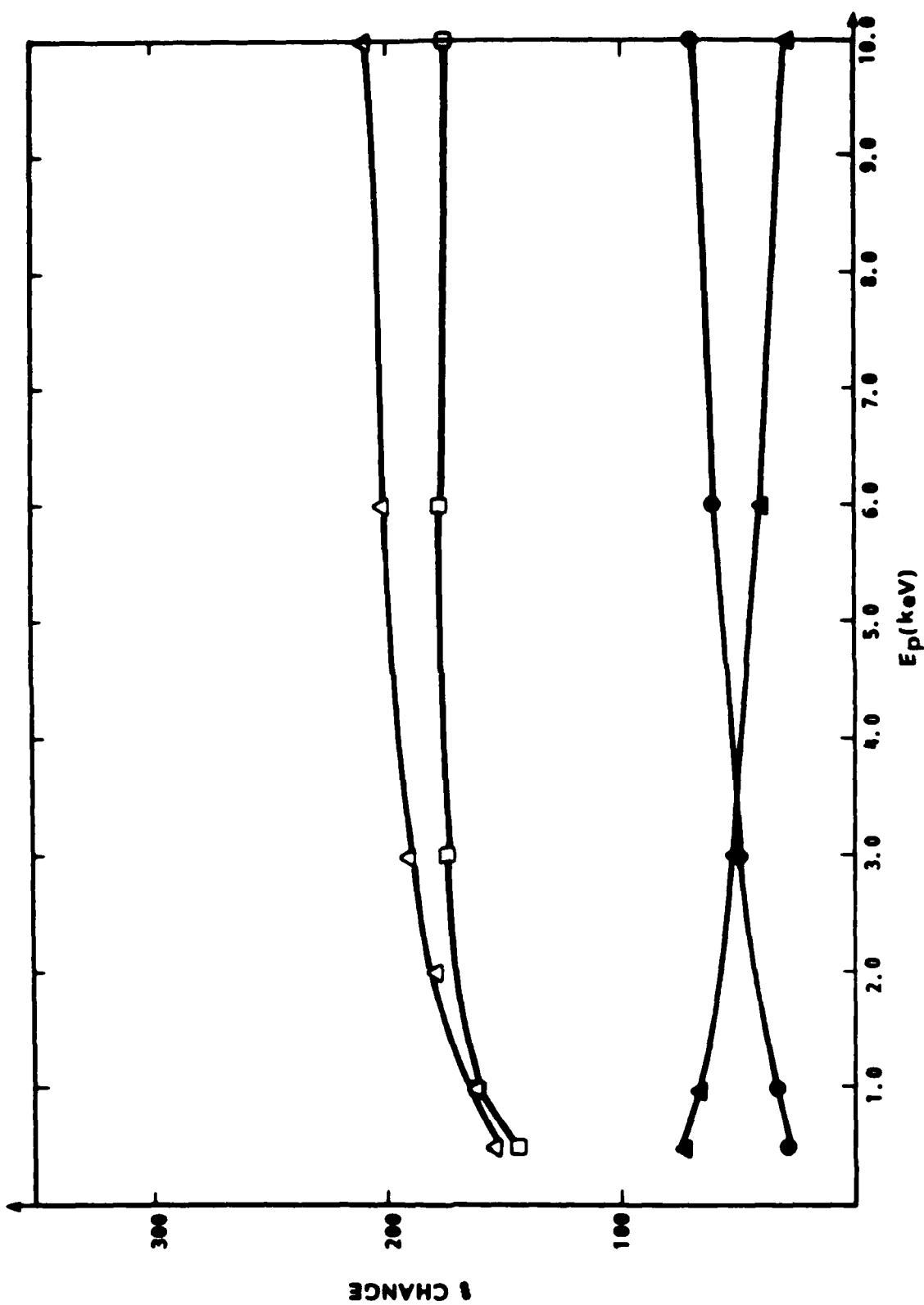
Fig. 10. Plotted results of MPI ratings and species percentages at normal incidence.

A final observation on yield versus primary energy, although not very useful for our purposes, may be seen from the results of experiments performed by Trump and van de Graaf.[15] Their results indicate that as the energy of a normally incident primary beam is increased to values on the order of 200 keV, both the total yield and the fast secondary yield asymptotically approach a constant. Since this trend was observed for several target metals, it is reasonable to assume that this is a common characteristic of all metals.

G. Emission Universality in Metals

Further support of the asymptotic approach of component yields in metals is the existence of several other commonly accepted universal emission properties of metals. As implied earlier, included in this list of properties is the energy distribution curve shown in Fig. 1. Although this curve has several characteristics common to all metals, the most obvious of these is the present and general characteristics of the two distinct enhanced emission regions.

The peak located in the first of these regions corresponds to the maximum yield of monoenergetic true secondaries. A series of measurements taken over the energy range defining region 1 of Fig. 1 was performed by R. Kollath[16] for 10 different metals. His results indicate that the difference in secondary energies at which this maximum occurs for metals is on the order of a 2 eV, and approximately centered at 2 eV.

A slightly more impressive result is the agreement displayed by metals over the entire slow secondary energy range of the measured

- 23 -

energy distributions. Figure 11, taken from Hachenberg et al.,[7] represents the spread of all recorded slow secondary distributions. As is
evident by the size of the shaded area, a high degree of conformity is
exhibited by all of the metals tested.
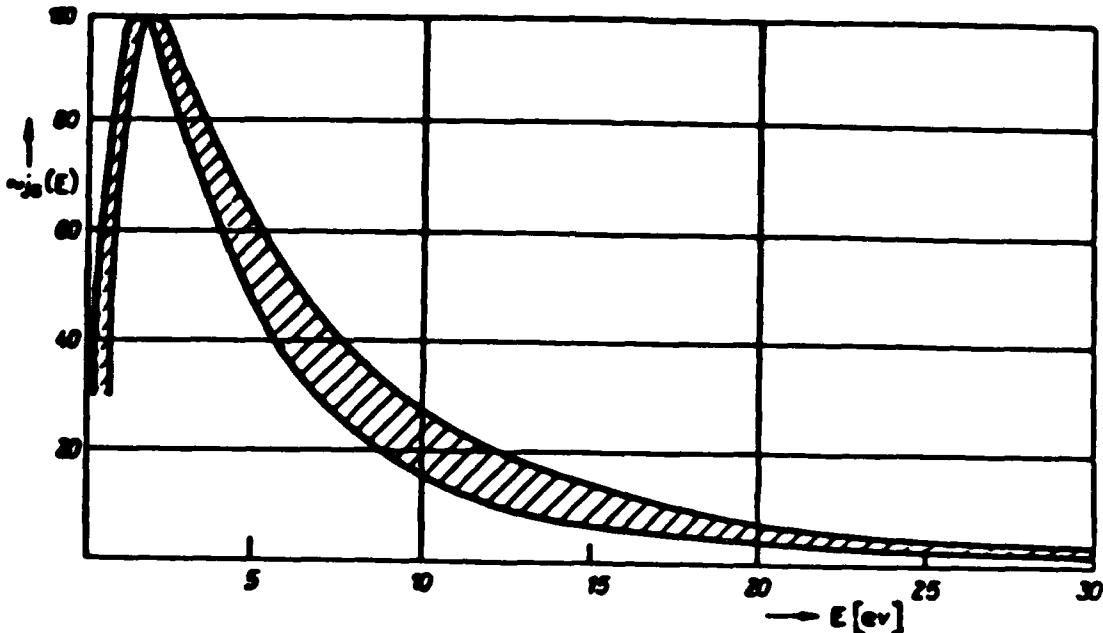
Fig. 11. Slow secondary energy spread for metals.

A second common characteristic of the energy distribution curve of
Fig. 1 is the presence of fine grain subsidiary maxima at slightly lower
energies than that of the high energy maximum located in the second
enhanced emission region. Rudberg[17] has shown for several metals that
the positions of these subsidiary peaks with respect to the peak of the
high-energy maximum are material specific and virtually independent of

primary energy over the energy range tested, $0 \text{ eV} < E_p < 400 \text{ eV}$. Since the subsidiary maxima are fine grain characteristics, however, their mention here serves more to emphasize the concept of metal universality than to provide direct secondary emission characteristics relevant to our model.

Perhaps the most widely-accepted universal emission characteristics of metals is the energy dependence on the total yield for a normally incident primary beam. Although the yield curves for metals generally have substantial differences in absolute terms, when plotted using a yield normalized to the maximum yield and a primary energy normalized to the primary energy for which the maximum yield occurs, excellent agreement between metal results. Figure 12, taken from Hachenberg et al.,[7] contains measured data for several metals after normalization. As is evident from this figure, a reasonably tight spread of normalized yields is maintained over the energy range plotted. Thus, the normalized yield has been considered a universal property of metals.

Although extensions of this property to primary beams at oblique incidence have not been verified experimentally for the lack of similar data corresponding to that of Fig. 12, it does seem likely that these inferences are in fact valid. One line of reasoning justifying this is as follows. As mentioned before, when subjected to a primary beam of variable incidence, polycrystalline copper experiences an increase in total yield, with the magnitude of this increase dependent on angular incidence and seemingly independent of primary energy, except at very low energies. Additionally, it should be noted that the general shape

- 25 -
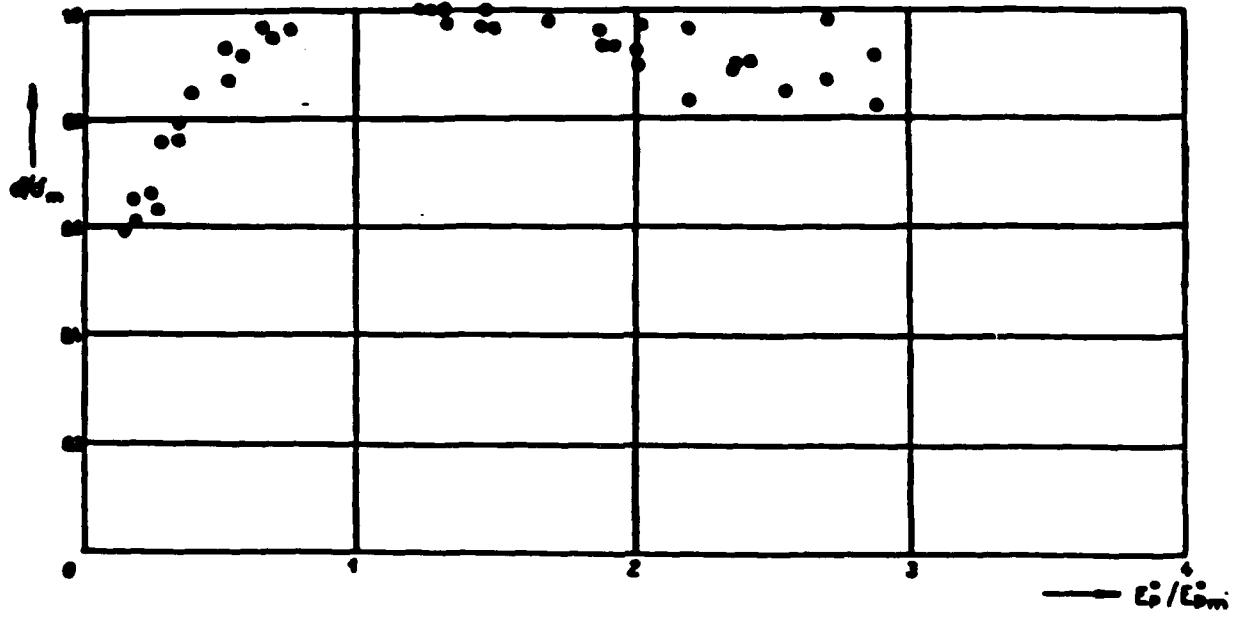
Fig. 12. Normalized yield versus normalized primary energy for metals.[7]

of the yield curve versus incident angle has been experimentally observed to be similar for all metals,[13] and that the aforementioned property of polycrystalline copper also appears to apply to other metals as well. Since the major difference in yield curves obtained by using a normally incident or an obliquely incident primary beam is an approximately constant yield increase over larger primary energies, the normalized yield curves, although different, will again be confined to tolerable limits.

There are two other observed emission characteristics of metals which are relevant to the secondary emission model being developed. The first of these is that the yield of metals is relatively independent of

- 26 -

primary current.[9] Since this property has been observed to be valid
over a variety of laboratory conditions, no further discussion of this
issue is needed.

Unlike the yield dependence on primary current, the second of the
above referenced characteristics common to metals has certain restric-
tions. Over certain temperature ranges, the yield of metals has been
shown to be relatively independent of temperature. Since the yield is
dependent on the work function of the emitting material, which in turn
is related to surface crystal structure and impurity concentration, this
property does not hold over temperature changes for which either of the
two preceding parameters has been significantly altered. These may not
be the only restrictions in order for this property to be valid, but at
present the author is unaware of any others.

Although this discussion has by no means covered all aspects of
secondary emission, it has covered most concepts needed to develop a
reasonable model. With this in mind, attention will be focused on the
task of developing a physically accurate secondary emission model.

III. SECONDARY EMISSION MODEL

A. General Considerations of the Emission Model

From the preceding discussion of the secondary emission character-
istics of metals due to electron bombardment, there are certain obvious
emission properties which must be considered in the development of any
emission model. The major of these being:

1. Yield and component yield variations with primary energy and
   incident angle.

2. Emission distribution variations with primary energy and
   incident angle.

3. Variation of the modeling process (due to both controllable
   and uncontrollable operating conditions).

Although all of the preceding properties of secondary emission are
important considerations in the model being developed, probably the most
important consideration is the range of PE conditions for which the
model is expected to perform. This is true, since this range not only
plays a major role in the model's overall range of validity, but also
the choice of modeling process used for the emission properties previ-
ously mentioned.

Since the emission model will be used primarily in TWT simula-
tions, it seems reasonable to require that the model be able to accu-
rately accommodate incident angles in the range $0° < \theta_1 < 90°$, as well
as primary energies in the range of $0 \text{ keV} < E_p < 10 \text{ keV}$. The upper
limit of 10 keV was chosen, since few TWTs operate with a cathode-to-
helix voltage exceeding 10 keV, and those that do generally operate

their collectors at depressions such that the beam is depressed below the 10 keV threshold when collected. In addition, the basic secondary emission data are not available above 10 keV. Although the model needs to be the most accurate in the domain defined above, provisions should also be made for PEs having initial conditions outside of this domain.

Acknowledging the trade off in model generality, much of the secondary emission model will be based on empirical data in order to accommodate the above range of PE initial conditions. Since these data are material dependent, a choice of target material is necessary. Because copper is one of the most commonly used TWT collector materials in industry today, empirical data for polycrystalline copper will be used when available. Instances in which appropriate data are not available for a copper target, similar data for a substitute material will be used. Fortunately, this is not expected to present a problem, since many referenced sources do use copper as the emitting material.

B. Component Yield Model Development

Two secondary emission parameters, which have been observed to change drastically over the range of PE incident angles, are the total and backscattered yields. As mentioned before, both are monotonically increasing functions with total yield increases on the order of 90 percent being typical for a 60° change in incident angle, and similar results applying to backscattered yields. Since the use of textured surfaces in order to reduce the component yield dependencies on incident angle is uncommon in today's TWT industry, the variation of yields with

incident angle, as mentioned before, should be included in the emission model.

Strong dependencies have also been observed for the yield components versus primary energy. Published results[8] show that for polycrystalline copper, the total yield may almost triple over the energy range 0.5 keV < E_p < 10 keV, with the backscattered coefficient decreasing nearly 50 percent over that same range. As in the case of yield cofficients with primary incidence, this relation should also be included in the model being developed.

The curves of Figs. 8 and 9, taken from Koshikawa et al.,[8] serve as the primary source for all data necessary to develop the required functional relationships existing between the component yields and PE initial conditions for polycrystalline copper. Rather than developing a two-variable expression relating these quantities, a number of single variable expressions were developed for fixed values of the second variable. Since the developed expressions are valid over a continuous domain of the first variable only, a further interpolation over the second variable is generally necessary for any given set of PE initial conditions.

Since the yield curves appear to be better behaved with angle than with energy, the yield coefficients were represented by using the primary energy as the continuous variable, and the incident angle as the interpolating variable. Additionally, since PE initial conditions are only approximate, as well as the fact that the yield curves are generally smooth over incident angle, any higher order interpolation over

incident angle would provide no better approximation than a linear interpolation.

A possible further benefit of using the linear interpolation, although not originally intended as such, deals with the sign of the predicted error. Since all yield curves shown exhibit the same nearly parabolic form, calculated values using linear interpolation will be slightly higher than values taken directly from the curves. Combining this observation with the fact that Kowhikawa and Shimizu mentioned that their measured backscattered coefficients for large angles of incidence may have been lower than actual yields due to the possible presence of stray fields in the measurement apparatus, it can be seen that the linear interpolation may result in a slightly more accurate backscattered coefficient.

In the case of the total yield, however, the increase in predicted value related to the interpolation is not expected to compensate for experimental errors, since these measurements are considered by the experimenters to be accurate. Thus, this process would return a slightly more erroneous slow secondary coefficient. However, due to the relatively low energy levels of the true secondaries and the relative strength of the retarding fields in most collection regions, the error introduced in the slow secondary yield is expected to be less detrimental to model operation in contrast to beneficial compensation noted for the fast secondary yield.

The angular step size chosen between successive component yield/ primary energy expressions was 5 degrees. The primary motivation behind this choice of step size was that it seemed to offer a reasonable

✗ /

trade-off between compactness and interpolation accuracy, assuming that the above assumption does not apply and that the data presented in Figs. 8 and 9 are valid.

As is evident from the preceding discussion, the structure of the above component yield model should allow for reasonable results, since the error introduced by this method of data storage and retrieval should be relatively minor compared to the error introduced by other aspects of collector simulation modeling to be discussed shortly. Although the structure of the model is sound, several conditions must be met in order to assure reasonable performance when this structure is implemented. The first of these is that the data published by Koshikawa and Shimizu are accurate, and the second is that a reasonable fit to the data may be made over both PE energy and incident angle.

Although the accuracy of Figs. 8 and 9 are slightly beyond our control, a rough idea as to the reliability of the model due to the data used may be obtained by comparison with other experimental results. Using the results of several experiments, McKay[9] indicated that most likely, maximum yield of copper for a normally incident beam is approximately 1.3 occurring for a PE energy of about 0.6 keV. The 0.5 keV yield curve presented by Koshikawa et al. suggests that the total yield at normal incidence is approximately 1.4, with the corresponding maximum yield possibly higher still. Since there are a number of subtle material variables which may directly affect the predicted yields, while not making the measurements valid, this 10 percent discrepancy in the maximum yields is not unrealistic or unacceptable in terms of the overall collector model.

Although this characteristic is not intended as conclusive proof that the data shown in Figs. 8 and 9 are accurate, this along with several other predicted trends, with both incident angle and energy, does indicate that these data are at least realistic. These trends will become more obvious once the component yield functional relationships are developed. However, in lieu of further evidence either proving or disproving the validity of Figs. 8 and 9, the data provided by Koshikawa et al. will be assumed accurate in the remainder of the thesis.

A second condition, which must be met in order for the component yield model to operate reasonably, is an accurate extrapolation of the reported data to the domains outside of those measured. Since measured data were only reported for incident angles in the range $0° < \theta_i < 65°$, with the larger angles of incidence changing most rapidly, the region $65° < \theta_i < 90°$ may contain significant extrapolation error. However, since all yield curves presented seem to be smooth and follow an almost quadratic relation over the incident angle range measured, a relation which from other researchers is expected to hold over larger angles of incidence as well, appreciable error is not expected to be much of a problem in the extrapolated region.

For each yield curve shown in Figs. 8 and 9, yield-angle data pairs were supplied to a least squares program. The order of the fitted equations was clamped to be at least one lower than the number of data pairs being fitted; and two types of equations, a polynominal in X and an exponential in X, were used as the form of the approximating equation. Invariably, as expected, all predicted best-fit equations were

- 33 -

polynomials in X, with generally only minor contributions made by third and higher order terms.

The resulting yield relations plotted over all incidence are shown in Figs. 13 and 14. The dashed curve in Fig. 13 was taken from reference 12 and represents a total yield curve for incident angles approximately reaching 78 degrees. Although the PE energy used in generating the curve is unknown, the similarity in shape to the adjacent curves serves to indicate that the method used for extrapolating the yield at larger angles of incidence gives reasonable results.

To complete the component yield model, equations relating the component yields to the primary energy were calculated in much the same way as those used for extrapolation to large incident angles. Two additional features were employed in the least squares fit routine in order to yield physical curve shapes. The first of these was to fit the data to a polynomial in 1/X, a relation which seemed applicable in view of the previously mentioned asymptotic character that physical yield curves exhibit at larger primary energies. The second of these was the method used in choosing the best fit equations.

A smoothing routine based on the null hypothesis[18] was also added to the least squares fit routine and a new set of equations was calculated. The resulting set of best fit equations was all polynomials in 1/X, found to be superior to polynomials in X. Several of the curves generated from these quations are shown in Figs. 15 and 16.
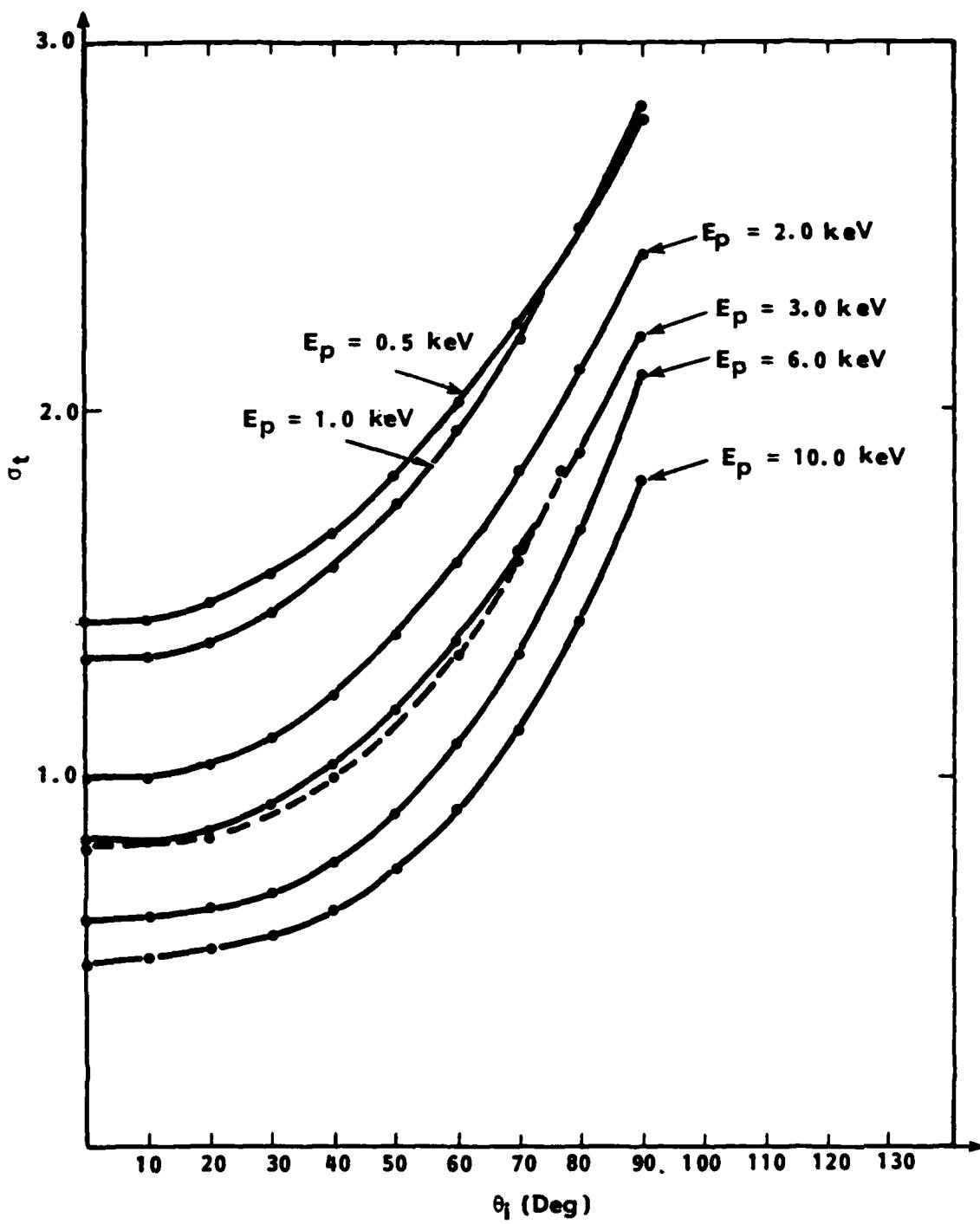
Fig. 13. Total yield curves extrapolated to grazing incidence using the results of Koshikawa and Shimizu[8] and compared to data found in reference 12 and originally reported by Muller.[12]

- 35 -
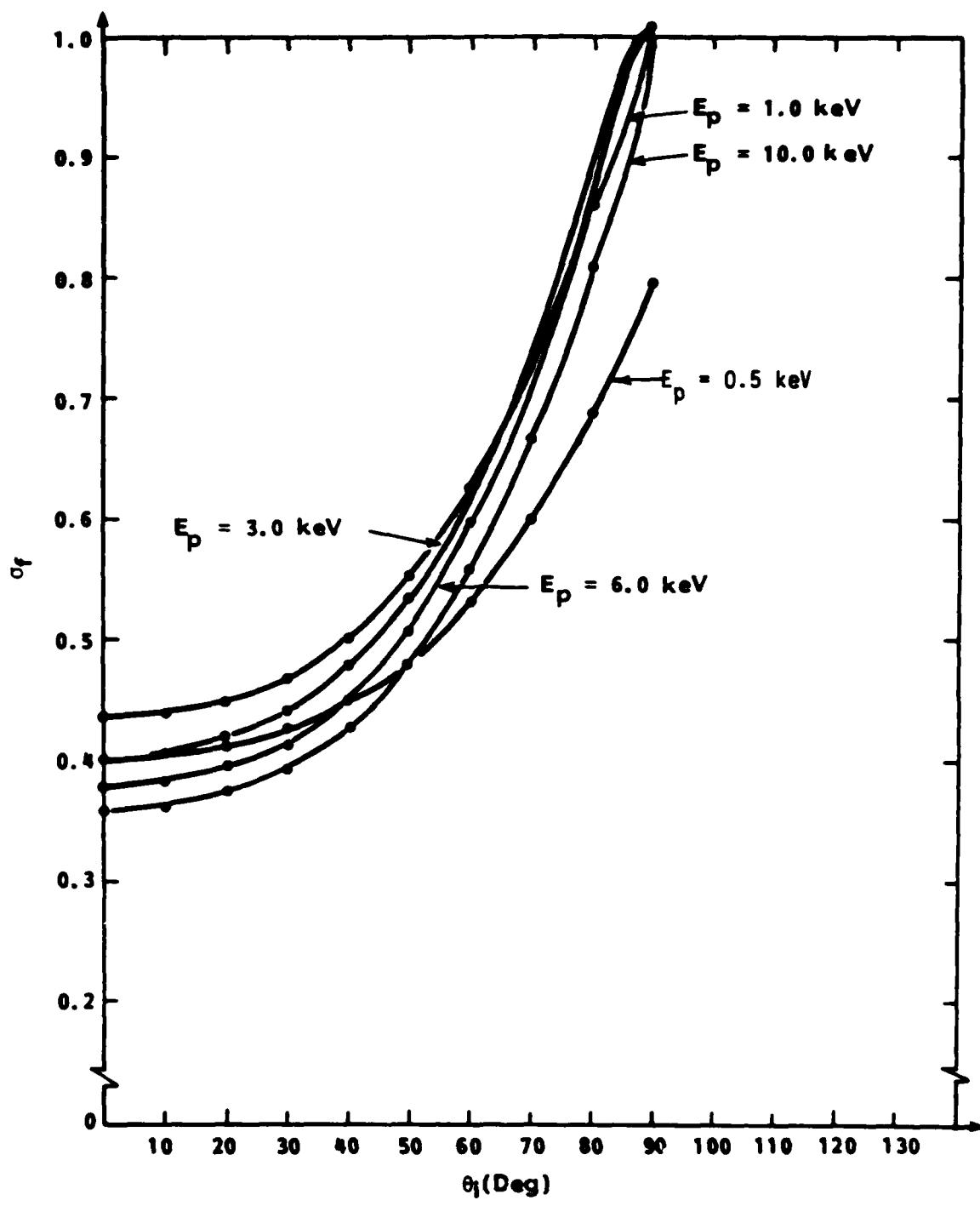
Fig. 14. Backscattered yield curves extrapolated to grazing
incidence using the results of Koshikawa and Shimizu.[8]

- 36 -
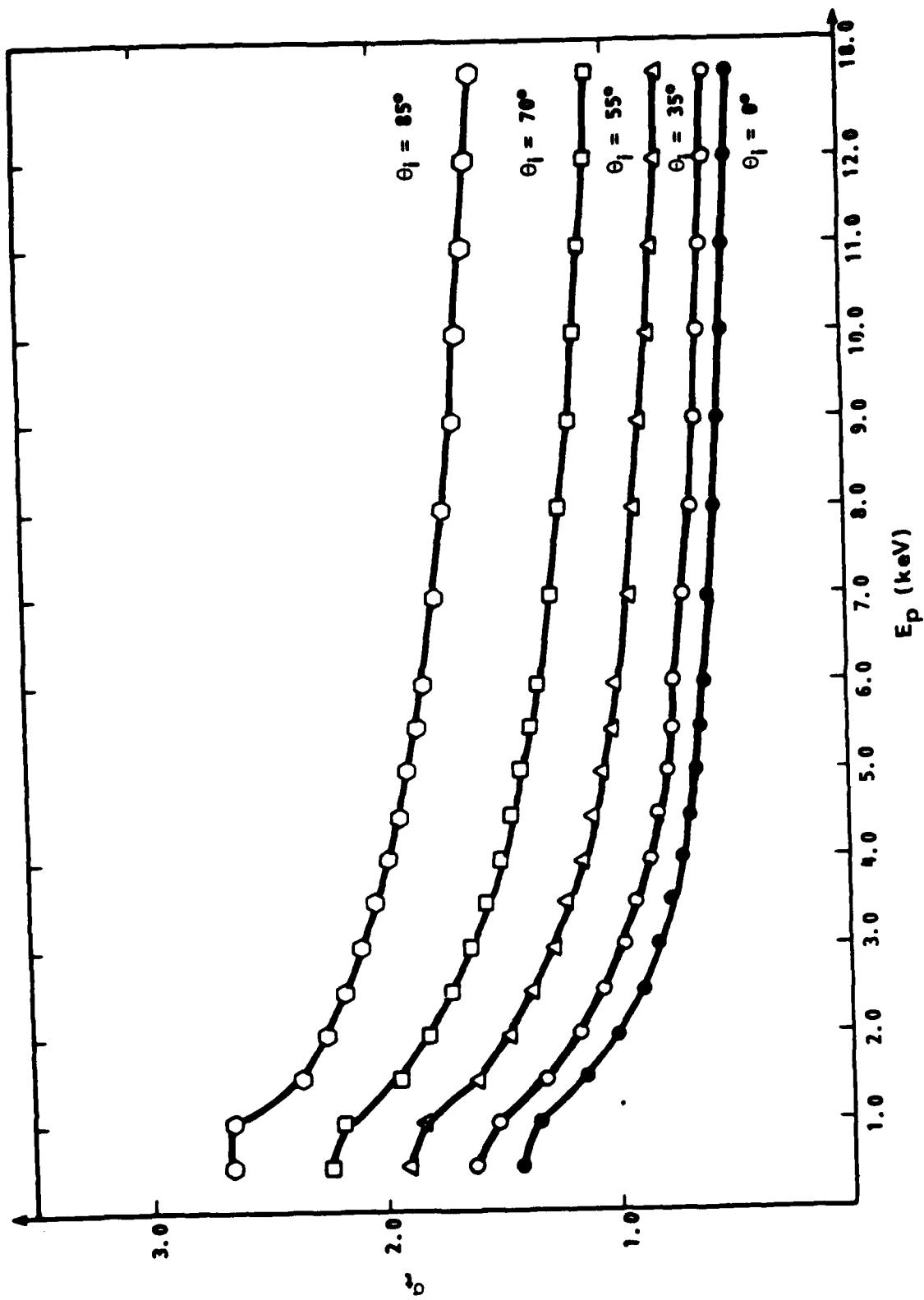
Fig. 15. Total yield curves generated using the total yield expressions developed for the emission model. These expressions were generated using the data presented in Fig. 13.
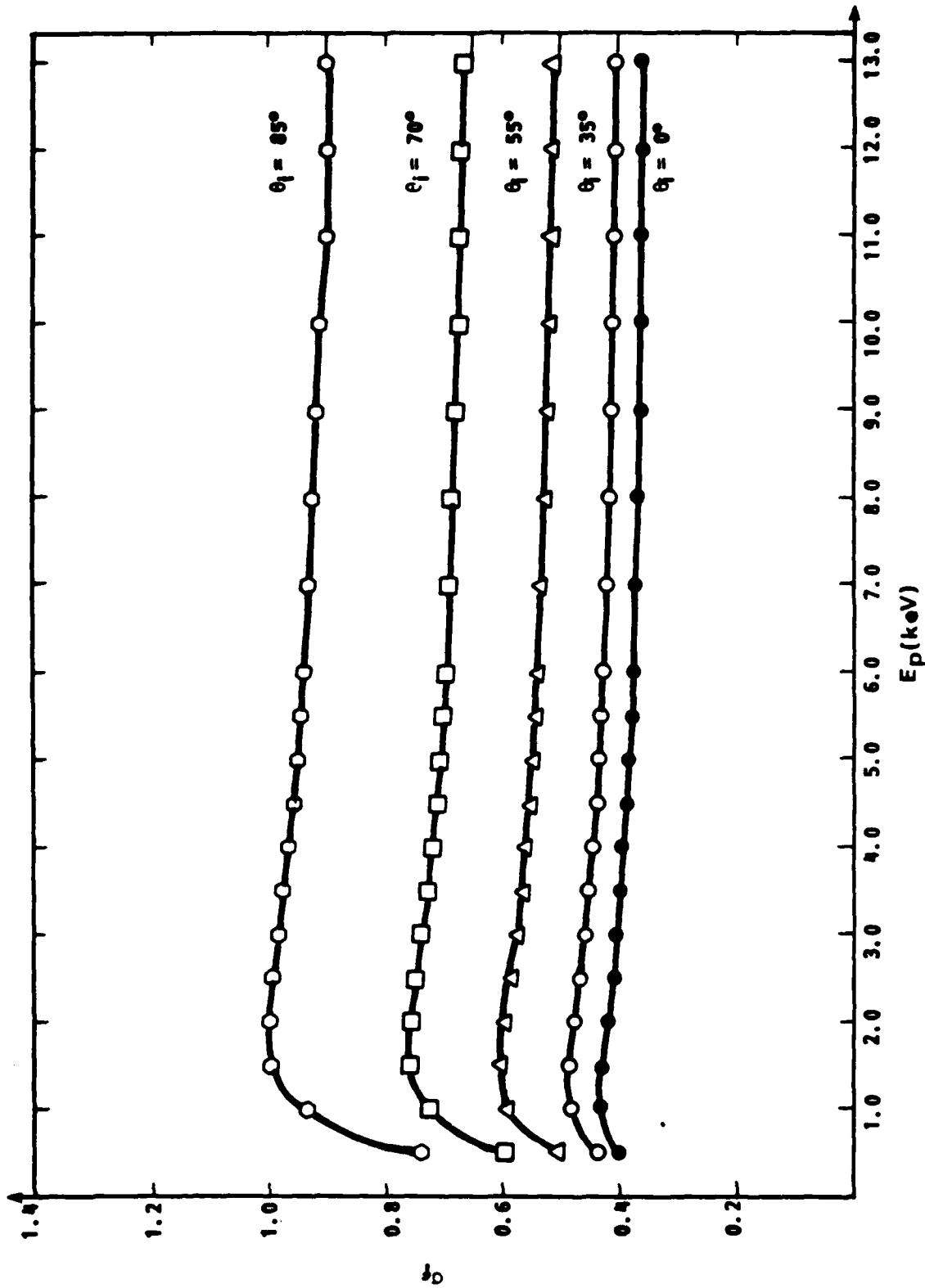
Fig. 16. Backscattered yield curves generated using the backscattered yield expressions developed for the emission model. These expressions were generated using the data presented in Fig. 14.

Certain features of these approximating curves appear to make this family of component yield curves a better choice for the component yield model. The first of these is the general shape of the total yield curves shown. As mentioned in the previous discussion, not only is this a universal characteristic of metals, but the relative shape is virtually independent of incident angle. A second characteristic of the approximating family of curves which merits noting is the smoothness over the energy range plotted.

C. Component Yield Model

Although the preceding characteristics would seemingly indicate that representing the component yields by polynomials in 1/X provides a good representation of physical values, characteristics of these curves also exist which limit the range of their validity, of which the most obvious occurs for small values of primary energy.

Because the approximating functions are polynomials in 1/X, component yields approach infinite values as the primary energy approaches zero. Since the yield must be finite, this representation is obviously invalid for very low primary energies, and thus a special adaptation is used in this range.

A second range of primary energies for which the derived relations are invalid is for high primary energies. This is due to slight discrepancies in asymptotic values of total yield and backscattered yield for the incidence of 5 degrees which, if left as is, would predict a small negative, slow secondary yield. Thus, this requires that

modification also be made in the component yield model for high primary energies as well.

Deterioration in the curve fits to the data was observed below 0.75 keV. To be conservative, the derived equations were assumed to be valid over the range 0.75 keV $< E_p <$ 10 keV. Note that the upper boundary of 10 keV was not established to be the upper limit for a consistent set of yield equations, but rather assumed, since empirical data were available only to that point. The resulting energy ranges with the component yield functions used in each region are shown in Fig. 17.

Several points can be made about the component yield model. First, the difference between the upper and lower boundaries of the cross-hatched region at any given primary energy is the slow secondary yield for a given primary energy. Expressed in a different way,

$$\sigma_t = \sigma_s + \sigma_f \qquad (5)$$

This point should be obvious from Eqs. 1-3.

A second point of interest is the alternate method used to determine the yield coefficients, and thus the component yields for primaries with energies less than 0.75 keV. As is obvious from the figure, the fast secondary yield is assumed to be constant for this region, assuming the same value at 0.75 keV. In this same region, the total yield tapers linearly from the backscattered value at a primary energy of 0 keV to the predicted value at 0.75 keV.

$\alpha_t(E_p) = \alpha_t(0.75\text{keV}) - (0.75-E_p)\text{keV}\ \dfrac{(\alpha_t(0.75\ \text{keV}) - \alpha_f(0.75\text{keV}))}{0.75\ \text{keV}}$

$\alpha_t(E_p)$

$\sigma_f(E_p)$

$\sigma_f(E_p) = \sigma_f(0.75\text{keV})$

$\sigma_t(E_p) = \sigma_t(10.0\text{keV})$

$\sigma_f(E_p) = \sigma_f(10.0\text{keV})$

1.0 2.0 3.0 4.0 5.0 6.0 7.0 8.0 9.0 10.0 11.0

0.75

$E_p(\text{keV})$
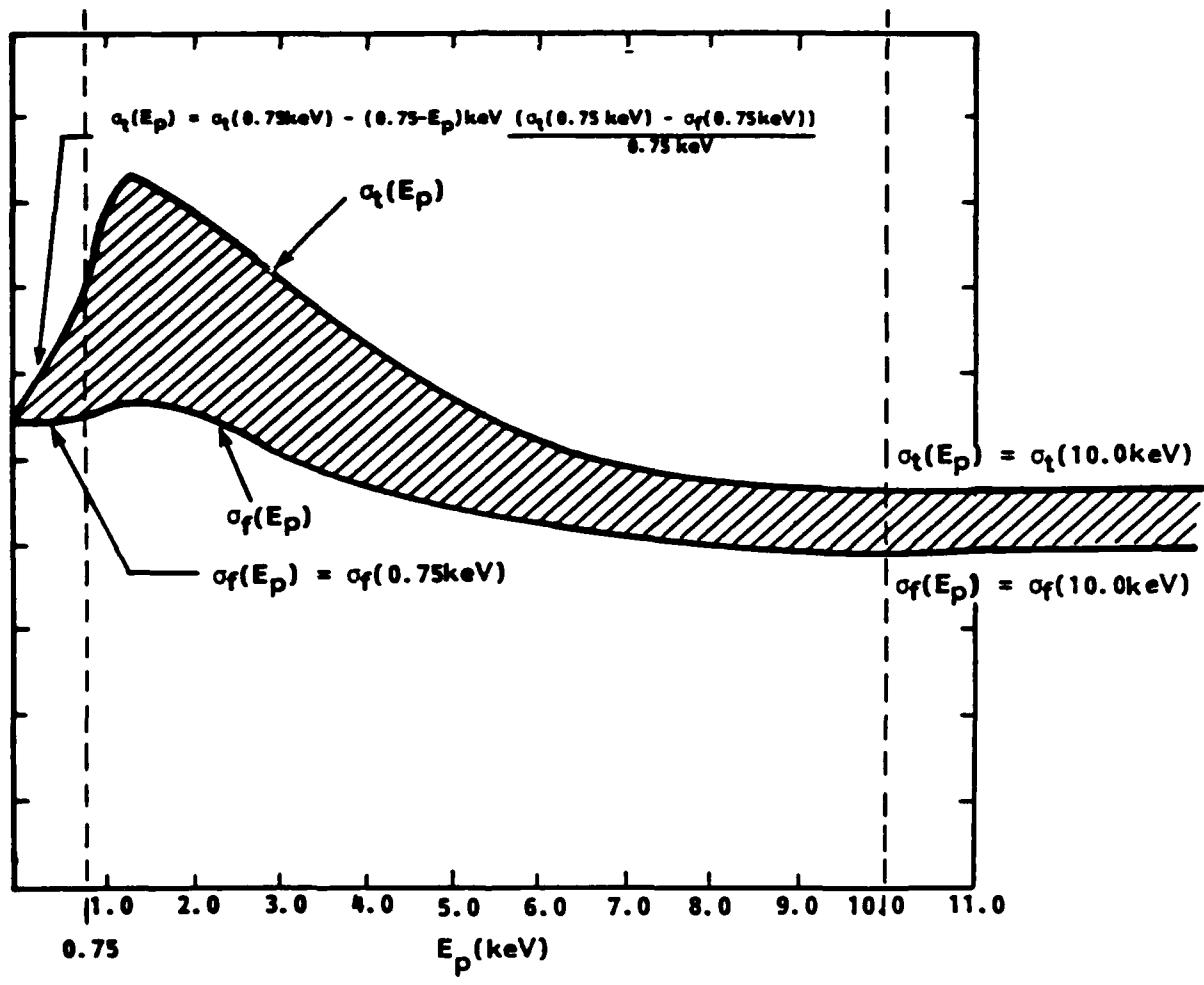
Fig. 17. The three distinct regions of yield modeling and
their respective values for total and backscattered
yields as used in the secondary emission model.

- 41 -

Several things motivated this choice of modeling for this region. First, while a finite yield is known to exist in the limit as the primary energy approaches 0 keV, the limiting value is unknown. Additionally, it is also known that the yield for very low energies is composed of a high percentage of fast secondaries, with this percentage increasing even further for further decreases in primary energy. This last trend continues until a primary energy of approximately 10 eV is reached, for which case the total yield and the fast secondary yield are approximately the same.[6] As can be seen from this, the model and the actual phenomenon are qualitatively, if not quantitatively, in agreement for this region.

A final point about the component yield model is the yield treatment for primary energies above 10 keV. For primary energies in this range, the component yields are assumed to have reached their asymptotic value, and are thus treated as constants. Even though the physical asymptotes are not actually approached until much larger primary energies, the approximation, as is the case of the low primary energy modeling, is not expected to increase the error substantially in the overall collector model, due to the relatively small number of electrons being collected with energies in this range for most TWT collector designs.

D. Component Yield Quantization

Along with the component yields, the emission model should include an emission angle dependence. This should be obvious in light of the previous discussion on emission distributions. As before, much of this modeling will be based on empirical data available for polycrystalline nickel.

Since the model is to be included in a computer simulation, some discrete representation of the observed continuous distribution is necessary. As mentioned earlier, the observed distributions of fast and slow secondary yield vary significantly, especially with solid angle of emission. It was thus decided that the broader of the two distributions, that of the slow secondaries, was to be represented by three rays, and that the relatively narrow fast secondary distribution would be represented by a single ray. The limit of four secondaries per primary was a prudent one in view of the enormous memory requirements and increased execution time for each additional ray.

As mentioned before, results published by Jonker show that it is reasonable to assume a cosinusoidal distribution for true secondaries, as shown in Fig. 2. Since three rays are to represent the true secondary emission, it is workable to ascribe to each ray one-third of the true secondary emission current. However, since the program used in the actual collector simulation is a two-dimensional code, the division of the total current into thirds will be restricted to the projected planar current and not the actual three-dimensional current. Since the

collector electrodes are assumed to be axially symmetric, this approach should provide a good first approximation to the actual distribution.

Appendix A contains a detailed derivation of the expression for the total planar current, with emission angles between θ_1 and θ_2. Since a closed-form solution could not be found, all integrations needed to be performed numerically. The numerical quadrature method chosen for all integrations was the trapezoidal rule with Richardson extrapolation.

The first integration performed was done over all emission angles so that the total planar current yield was known. This value was then used as a normalization factor for subsequent integration.

Since the division of current elements into thirds provides a method for distributing the secondary yield, but not the emission angle of each component, it was decided that each third would be emitted at the median angle of its respective wedge section. By definition, one of these would be the direction normal to the surface, however, the other two are not so obvious. Thus, an iteration employing bisection of the integration range was used in determining these remaining launch angles. The resultant discrete distribution of slow secondaries used in the emission models is shown in Fig. 18.
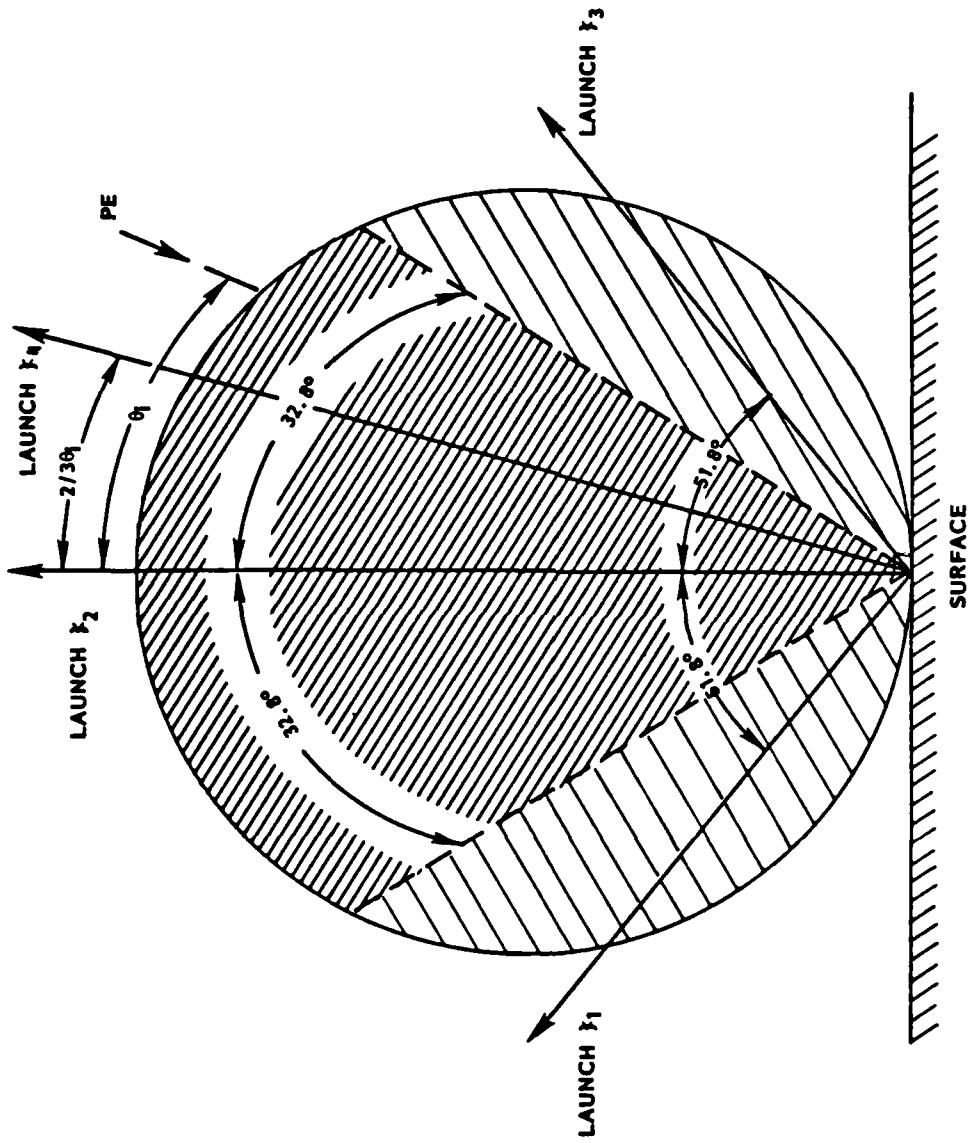
Fig. 18. Launch angles for the quantized yields used in the secondary emission model. Launch angles 1, 2, and 3 represent the three emission angles for slow secondaries. Launch angle 4 represents the emission angle for the backscattered yield.

Determining the emission angle for the fast secondary yield is
much more straightforward.   Table 3 contains a tabulated version of
Jonker's measurements for fast secondary distributions.   In many of the
distributions presented by Jonker, the distribution maximum serves as an
approximate axis of symmetry as well; thus, the angle of maximum emis-
sion was chosen as the single direction of fast secondary emission.   For
most of the values presented in the table, the emission angle is approx-
imately 2/3 of the incident angle, regardless of primary energy.   Thus,
a phenomenological adaptation is made for setting the fast secondary
launch angle, despite the lack of adequate physical explanation for its
occurrence.

Table 3.   Tabulated fast secondary emission angle as taken from Jonker.

PE Incident <	PE Incident Energy	SE Maximum Emission <	PE Incident < SE Maximum Emission
0°	25 V	0°	?
0°	100 V	0°	?
0°	450 V	0°	?
30°	25 V	18°	0.60
30°	100 V	36°	1.20
30°	450 V	16°	0.53
45°	25 V	32°	0.71
45°	100 V	33°	0.73
45°	450 V	30°	0.67

E. Emission Model Stability with Operating Conditions

Since TWTs, as well as a number of other electron devices which require electron collection, are subject to a variety of operating conditions, it is important to examine the effects of the emission model's flexibility and reliability with changes in operating conditions. For several reasons, primary current and temperature may vary considerably in both time and space for any given device or collector. Since these parameters are not easily controllable by appropriate collector design, the effects of these on the model are relevant, and thus their impact as related to TWT collectors will be discussed.

By their very nature, TWTs modulate the current and velocity of an electron beam in extracting energy from it. Noting that the beam current varies for different applications as well, a further scaling of primary current entering the collector may result. Since the current entering the collector is time dependent, it is intuitively obvious that collected primary currents would also differ significantly with both time and space. As discussed before, however, metals exhibit a universal tendency to maintain relatively constant yield characteristics with PE current, thus variaitons in PE current are not believed to be directly responsible for errors in the emission model.

What is true, however, is that temporal and spatial variations in primary current, as well as the ambient temperature of the device, set up temperature gradients over the collection surface. Pulsed devices working on the principle of electron beam switching further complicate matters in that they may make these gradients a stronger function with

- 47 -

time. As before, however, it has been shown that yield characteristics of metals are virtually independent of temperatures. All of this leads to the conclusion that temperature and current densities, which are not easily controllable in practice, fortunately are not expected to adversely affect the model's performance in simulating physical collectors.

Although other operating conditions may exist, which do in fact affect the performance of the emission model, these are not apparent to the author. Thus, it is concluded that no discrepancy between actual and modeled yield data will be solely the result of operating conditions. The final consideration of the secondary emission model to be discussed is its range of validity.

F. Range of Validity

Since much of the emission model previously developed has its basis in empirical data, certain conditions must be satisfied in order for the emission model to be valid. The first of these is that whatever the target material being used, it must exhibit similar yield tendencies versus incidence and primary energy. The second is that the surface be of comparable smoothness as the sample used in obtaining the data. Finally, the target material should be a metal (or else operating conditions may change the performance of the model).

If the above conditions are met, a further embellishment, a yield scaling factor, has been added to the emission model. For similar metals (i.e., copper and nickel), this feature appears to be useful; however, extension to other suitable collector electrode materials may

be inappropriate more often than not. For these metals, a more elaborate normalization of the curves would prove worthwhile. Possible areas of further adaptation of this model may involve an inclusion of normalized yield, as previously discussed. Alternately, a normalization of yield data with angle of incidence may be explored, possibly by using the MPI figure previously defined, or some other method. These, however, will not be included in our emission model; and thus, the validity of our model is limited to the restrictions previously mentioned.

IV. COLLECTOR ANALYSIS MODEL

A. Introduction to the Analysis Model

As may be seen from the previous discussions, an improved second-ary emission model by itself is not enough to ensure good MDC simula-tion. Not only is this true, but the addition of a more accurate emis-sion model may actually make analytical analysis of collectors less accurate, resulting from an increased significance of PE incidence and energy. This point demonstrates the need for certain inclusions in the total collector analysis model to ensure at least a reasonable represen-tation of PE trajectories upon collection.

Due to the generally favorable success of the LRC model, the overall approach of collector simulation used in that model will also be used in this one. As a consequence of this, the simulation will be approached as a two-stage process; the first of these being the modeling of the beam from the RF input of the TWT to the entrance of the collec-tor, or the interaction region, and the second being the simulation of the beam in the MDC region.

For the most part, the modeling of the individual regions will also be paralleled with that of the LRC model. Thus, with only few exceptions, all features of the LRC models are also included in the models used in this simulation. Additionally, several other features, not specifically acknowledged as being included in the LRC model, have also been incorporated into the RF interaction simulation.

B. RF Interaction Region Modeling

For the purposes of determining a PE initial condition profile upon entrance into the MDC, a large signal program which computes both RF power and beam data was employed. A version of the large signal program employed by Dayton et al. was used for this RF region modeling. In way of a brief description, this simulated beam-RF interaction was based on J. E. Rowe's[19,20] nonlinear interaction theory developed for a traveling-wave amplifier. Other considerations provided for the LRC model are:

1. The introduction of RF circuit losses.

2. Provisions for attenuators and severs.

3. User definable phase velocity and circuit impedance.

4. User definable variable circuit radius.

5. Simple and complex PPM focusing.

6. Relativistic correction to the axial equation of motion.

7. The use of the complete second order circuit equations for the RF wave.

8. The retention of all terms involving C (the square of Pierce's gain parameter).

9. Optional number of deformable disks or rings used in modeling the electron beam.

10. The use of the hot phase velocity for the beam loaded RF wave.

11. The optional inclusion of a backward wave.

In addition to the above, the large signal program used in this modeling also provided for:

12. The optional inclusion of multiple forward waves.

13. The relativistic correction to all equations of motion.

14. An energy conservation algorithm to facilitate an energy conserving electron beam.

One of the major influences on the trajectories of the individual electrons comprising the electron beam is the total power extracted from it. Thus, the difference between measured extracted power and that predicted by the large signal gain program was used as a measure of how well the predicted spent beam approximated the physical one. An interaction of inputs to the large signal gain program was performed until an accurate extracted power was achieved. Throughout the course of this interaction, only parameters assumed not to be known accurately were varied. Included in these are the phase velocity, attenuation, and interaction impedance.

C. Collector Region Modeling

Simulation of the collector region was accomplished by using a slightly modified version of an electron gun program originally developed by N. J. Dionne and J. J. Krahn[21] for the Naval Research Laboratory. In turn, this program had its origins in the Kirstein-Hornsby electron gun program.

The approach used to generate electron trajectories is to approximate the path traveled by the charge groups as a series of straight line segments in two dimensions. This ballistic approach, which involves the

determination of the kinematic equations, is then used in determining the charge group's new position assuming a finite travel time. The process is then repeated until the charge group is collected.

The major features of this collector model include:

1. The use of maganetostatic, electrostatic, and space-charge force terms (assumed axially symmetric) in the calculation of all kinematic equations of motion.

2. A finite travel time step, small in relation to the RF period.

3. The use of the secondary emission model developed earlier.

4. An energy conservative treatment of the collection of primaries.

5. An option to run fast secondaries only, slow secondaries only, both species of secondaries, or no secondaries.

6. The optional inclusion of multiple bounces of secondaries when any single species option of secondaries is employed (slow secondaries are then represented as a single current ray instead of the three current rays used when both species of secondaries are employed).

Incorporation of the space-charge forces into the collector model raises several questions as to the validity of an underlying assumption implicit in the collector code. Since the beam in the gun region is not bunched axially, it is reasonable to assume that a dc current exists for gun analysis. Thus, it was assumed that the discrete charge groups may be replaced by continuous current rays. Although reasonable for gun analysis, this approximation does not strictly hold for collector simulation.

- 53 -

Since the space-charge forces may contain some RF component due to the velocity modulated beam, the use of a continuous current ray will at best approximate the time averaged RF space-charge effects on predicted trajectories. However, it is felt that the use of this resultant quasi-steady-state solution will provide a sufficiently accurate simulation.

One final point of interest is the conversion of the time dependent output of the large signal gain program to the steady-state conditions required for the collector simulation. All time dependence was eliminated by an axial shift of all charge rings to a common plane. During this shift, however, the magnetic flux referenced back to the cathode is not necessarily conserved. Thus, appropriate measures were also taken in calculating the radial coordinates to ensure that the resulting data still conserve magnetic flux.

V. COLLECTOR MODEL PERFORMANCE

A. Single Bounce Secondary Model Performance with Varying Spike

The accuracy of the collector simulation model was examined by comparison of predicted and measured collected current distributions for an existing continuous wave TWT. The TWT used for verification incorporated a two-stage MDC, with all collecting surfaces being either nickel or nickel plated. One concern in using this tube was that its geometry ensured that a slightly nonsymmetric magnetic field existed in the collector region.

Other basic operating characteristics of the TWT are as follows:

Operating bandwidth	7.6 GHz
Beam current	0.240 A
Beam voltage	10.15 kV
Maximum output power	275 W
Beam focusing	PPM
First stage depression	49 percent
Second stage depression	72 percent
Spike depression	100 percent

All verification runs were made at the single frequency of 10.4 GHz. Additionally, a saturated mode of tube operation was employed in all of the simulations.

The angular and kinetic energy distributions of the modeled saturated beam used are shown in Fig. 19. Evident from the figure is that a reasonably large range of particle trajectories exists at this entrance

SPENT BEAM ENERGY DISTRIBUTION
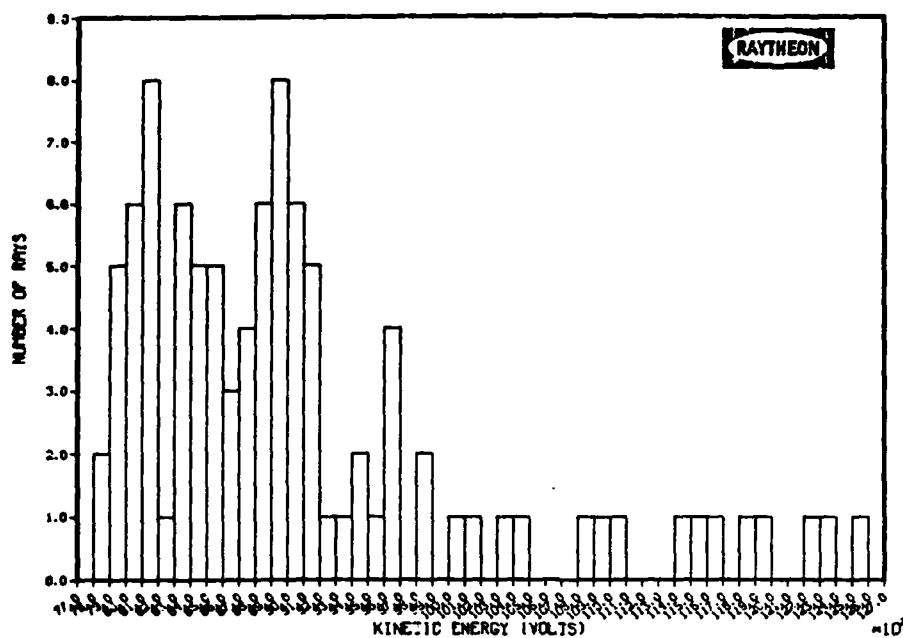
(a) Energy distributions given as a percentage
    of the original beam kinetic energy.

SPENT BEAM ANGULAR CLASS DISTRIBUTION
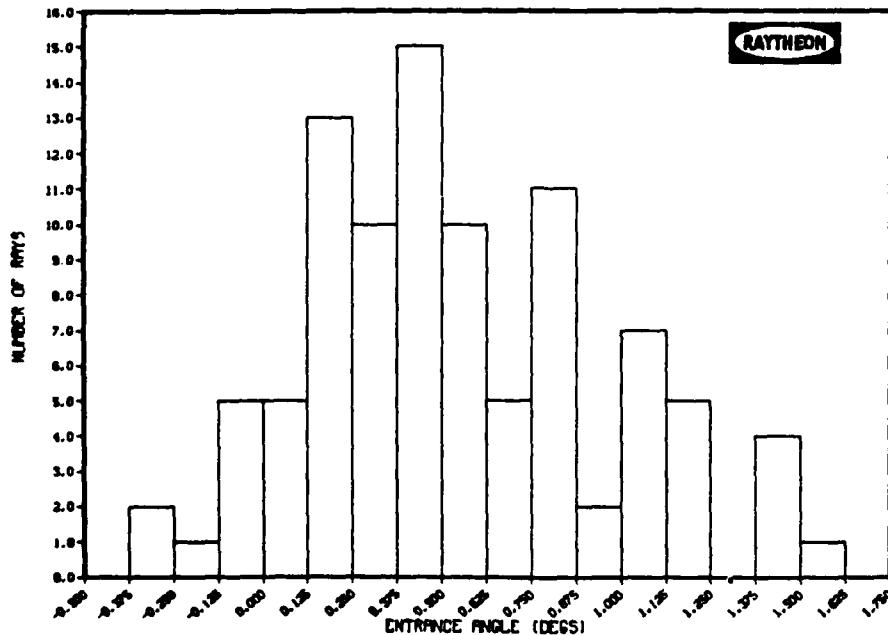
(b) Angular distributions given as the angle between
    the electron trajectory and the axis of the TWT.

Fig. 19. Spent beam distributions upon entrance into the collector
simulation program used for model verification.

plane. Consequently, an even wider range of trajectories is expected to exist at the points of collection. By utilizing this enlarged domain of the secondary emission model, a reduction in the cumulative error of collected current distributions introduced by the emission model for any individual ray should be realized.

Although in the preceding context, statistical averaging offers more insight into overall model performance, limitations to this approach also exist. The most notable of these is the strong RF component of beam current also associated with a saturated mode of operation and neglected in our modeling process.

For a 10.4 GHz signal, the periodicity of the beam current is approximately

$$T_b \simeq 1/10.4 \times 10^9 \simeq 9.615 \times 10^{-11} \text{ s}$$

Also noting that the axial dimension, d_a, of the collector being modeled is on the order of 0.06 meters, the transit time for a typical electron in the collector may be roughly approximated as

$$T_{trans} = \simeq d_a/v_{avg} \simeq d_a/\sqrt{2\eta V} \simeq 1 \times 10^{-9} \text{ s}$$

By virtue of the relative magnitudes of these times, a significant number of RF beam bunches may be present in the collector at any instant. Thus, predicted current distributions may be considerably different from experimentally observed distributions.

To mitigate the consequences of this, verification was performed using curves rather than a point by point comparison. The initial verification was generated by varying the spike potential. Since changes in the spike potential do not greatly alter the fields where the bunching effect is most pronounced, the entrance to the collector, the error in computed trajectories due to the omission of RF beam bunching in our modeling, should remain somewhat constant over the range of spike potentials plotted. Correlations between measured and predicted curve shapes should then provide a measure of how well the emission model performs.

Figure 20 shows the current distributions obtained by three methods; one method being measured data and the other two constructed from simulations.

In order to make the measurements on an unpackaged tube, the tube was operated at a greatly reduced duty cycle of 0.1 percent. A 10 μs pulse width was also used to ensure that any transient beam effects are negligible in the measurements.

The initial runs incorporated a yield scaling factor of 1, since nickel and copper have similar maximum yields at normal incidence.[9] In each of the curves generated for the individual stages, some qualitative similarity to measured results is evident above spike voltages of 2500 volts.

Although, in this range, the magnitudes of this set of generated curves differ dramatically from the empirical curves, both sets of curves exhibit maxima and minima at approximately the same locations. The most interesting of these being the minimum, which occurs in the
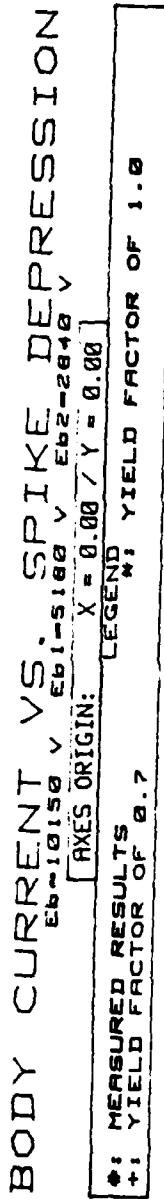
(a) Body current versus spike depression.

Fig. 20. Measured and predicted curves of current versus spike depression used in the emission model verification.
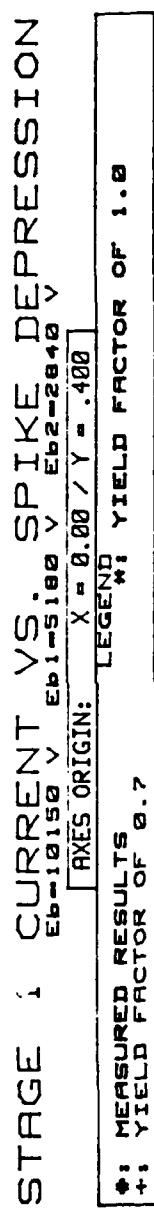
(b) First stake current versus spike depression.

Fig. 20. Continued

STAGE 2 CURRENT VS. SPIKE DEPRESSION
Eb=10150 v Eb1=5100 v Eb2=2840 v

AXES ORIGIN: X = 0.00 / Y = .700

*: MEASURED RESULTS   LEGEND
+: YIELD FACTOR OF 0.7   *: YIELD FACTOR OF 1.0

Ib2
(×10² mA)

2.00

1.00

Es
(×10³)

1.00   2.00
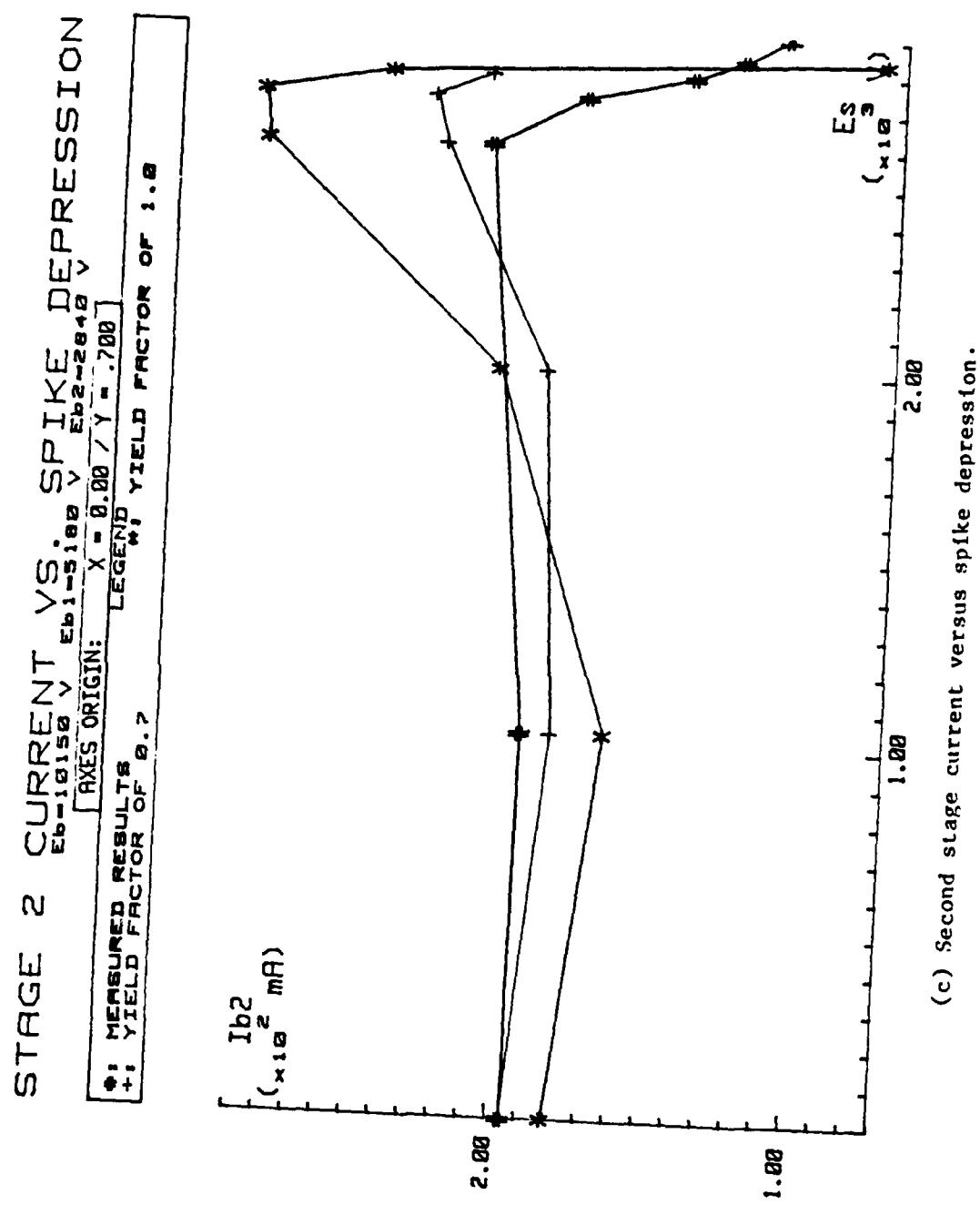
(c) Second stage current versus spike depression.

Fig. 20. Continued

- 61 -
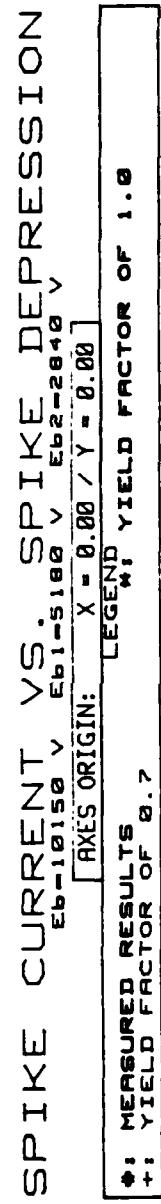
(d) Spike current versus spike depression.

Fig. 20. Continued

spike current I_s. For this region, both experimental and predicted results indicate that the spike acts as an emitter.

For the range of spike voltages below 2500 V, however, predicted results do not appear to agree quite as well with measured distributions, either quantitatively or qualitatively. This is most evident in the body and first stage currents, I_{ws} and I_{b1}, respectively, where current variations in excess of 45 percent of an expected constant value are predicted.

Consideration of the magnitude of the spike current, I_s, in the region where the spike acts as an emitter suggests that the simulations may be overoptimistic in their predicted yields. A second set of verification curves was generated using a scaling coefficient of 0.7 in order to examine this possibility. The results of these simulations are represented by the remaining set of curves shown in Fig. 20.

As in the first set of distributions, there are obvious similarities between the shapes of the predicted and measured curves, especially for lower values of spike depression. Additionally, although not readily observable from the curves presented in this form, similarity to measured distributions hold better at higher spike depressions as well.

Summing the body and first stage currents yields the curves shown in Fig. 21. As in the case of the individual currents, measurements indicate a reasonably constant current for spike depressions greater than 80 percent. On the other hand, predictions made using a scaling factor of 1 indicate that a significant variation in the combined currents over this range of spike depression will result, this variation being on the order of 20 percent of the measured value. However, for

- 63 -
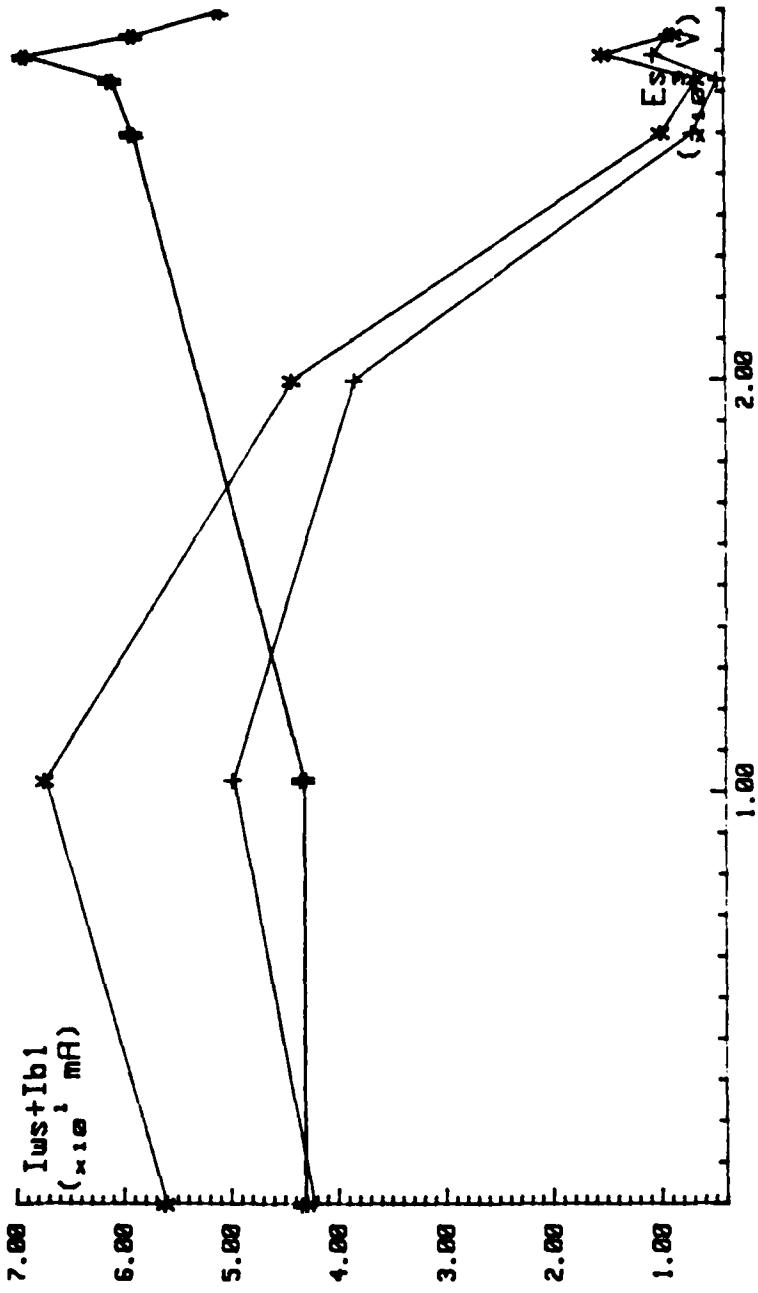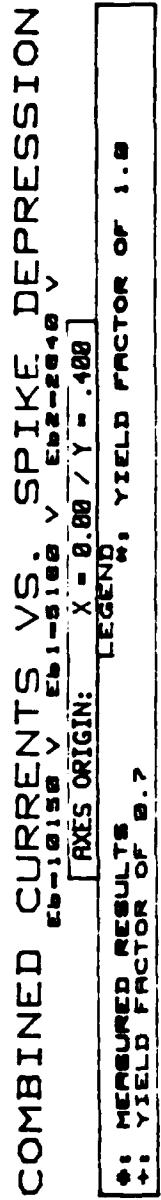
Fig. 21. Combined body and first stage currents versus spike depression generated using Figs. 20a and 20b.

similar curves generated using a scaling factor of 0.7, this variation is reduced to roughly 10 percent. Furthermore, the absolute accuracy of the predictions in this range was also significantly improved.

There are several possibilities why a reduced yield proved to yield slightly better results than the yield which would seemingly be accurate for the nickel collection surfaces of the collector used, the most probable being the macroscopic texture of the collecting surface.

Current and Fox[13] have shown that through suitable surface texturing, the yield of the emitting material may be reduced. The target surface used in obtaining the copper yield data was first polished mechanically, electrolytically, and finally cleaned by argon-ion bombardment, resulting in a surface texture similar to that shown in Fig. 22a. On the other hand, the machined parts making up the collecting surfaces would probably have a surface texture similar to that shown in Fig. 22b.

A second possibility is that the secondary lobe previously discussed as being observed, but ignored in the backscattered distribution, does in fact govern an appreciable amount of the backscattered current. Since the net effect of including this forward-directed current would almost certainly be a net decrease in the current deposited at lesser depressed stages, this is also a very plausible explanation.

(a) Sputtered copper surface   (b) As-machined copper surface. X1000.
having cones. X1000.
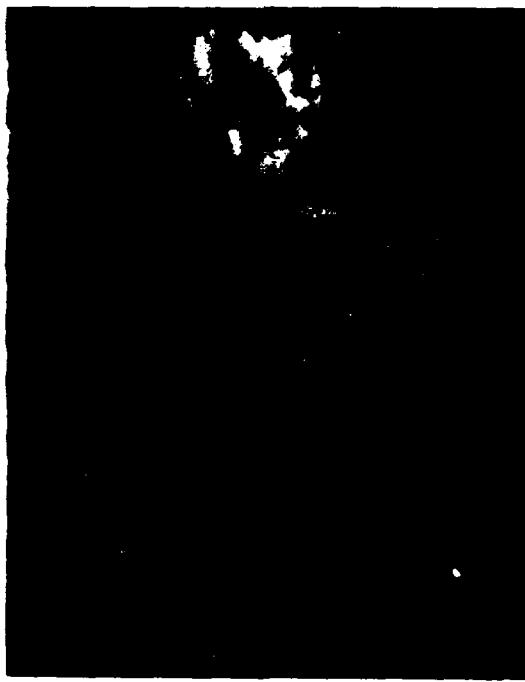
(c) Sputtered copper surface having needle-like protuberances.

Fig. 22. Scanning electron micrographs of copper surfaces showing texture.[22]

And finally, a third source of error may be introduced by the emission of higher order secondary yield. Figure 23 shows the predicted trajectories for each pair of the points comprising the 0.7 yield scaling distributions. It should be evident from these figures that at least some portion of the tertiary and higher order secondary yield will propagate toward higher depressed stages, effectively reducing the yield if only secondaries are considered in the analysis, at least for larger values of spike depression.

Note that the omission of the higher order secondaries may also be the primary cause of the body and first stage currents for depressed spike potentials, since for this case there is less of a retarding field in the vicinity of secondary collection, thus allowing backscattered as well as true tertiary and higher order secondaries to be emitted. Since the slow secondaries are low energy electrons, it is almost assured that they will either be recollected somewhere on the emitting electrode or at even less depressed stages. This, coupled with the relative size of the slow secondary yield, could lead to a significant secondary migration to less depressed stages.
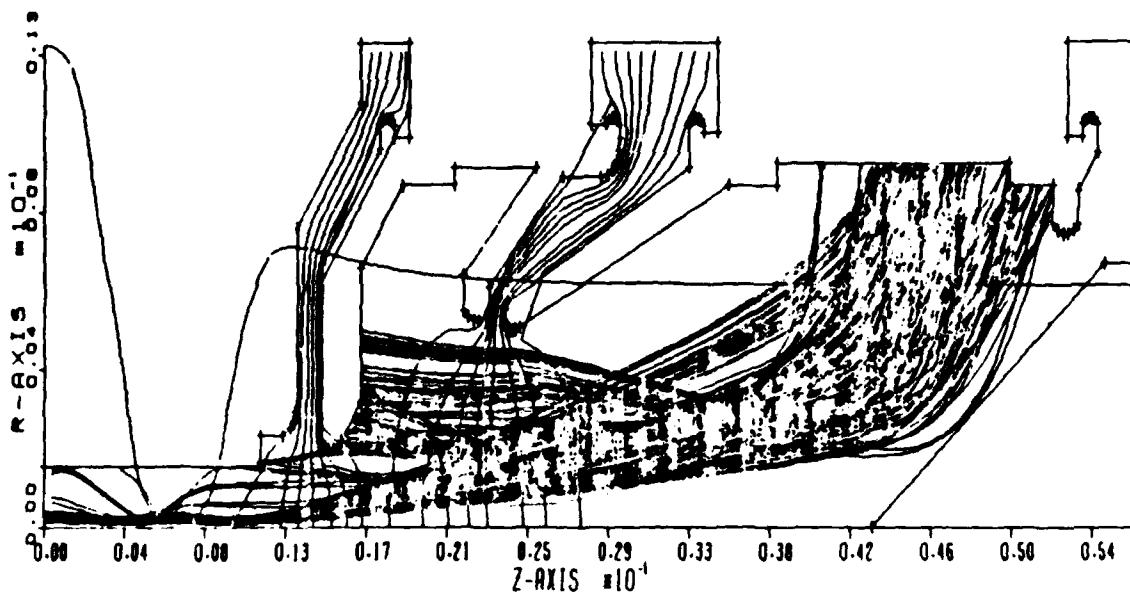
(a) $E_b = 10,150$ V, $E_{b1} = 5180$ V, $E_{b2} = 2840$ V,
and $E_s = 0$ V, all with respect to cathode.
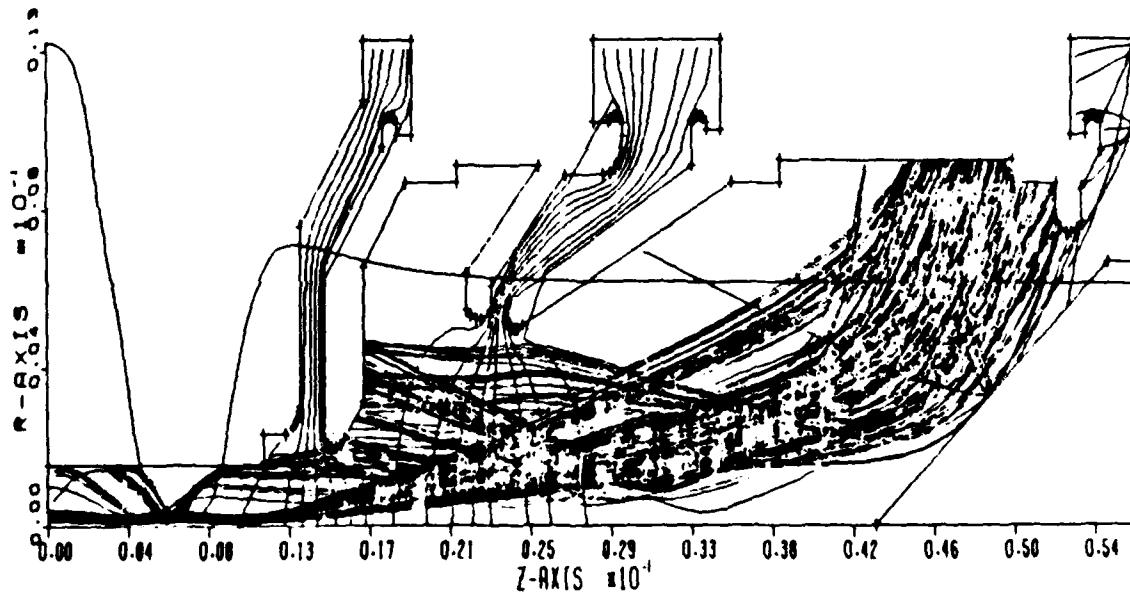
(b) $E_b = 10,150$ V, $E_{b1} = 5180$ V, $E_{b2} = 2840$ V,
and $E_s = 1030$ V, all with respect to cathode.

Fig. 23. Simulated paths of primaries and secondaries for a yield
scaling coefficient of 0.7 and all electrode potential
combinations used in generating Figs. 20 and 21.
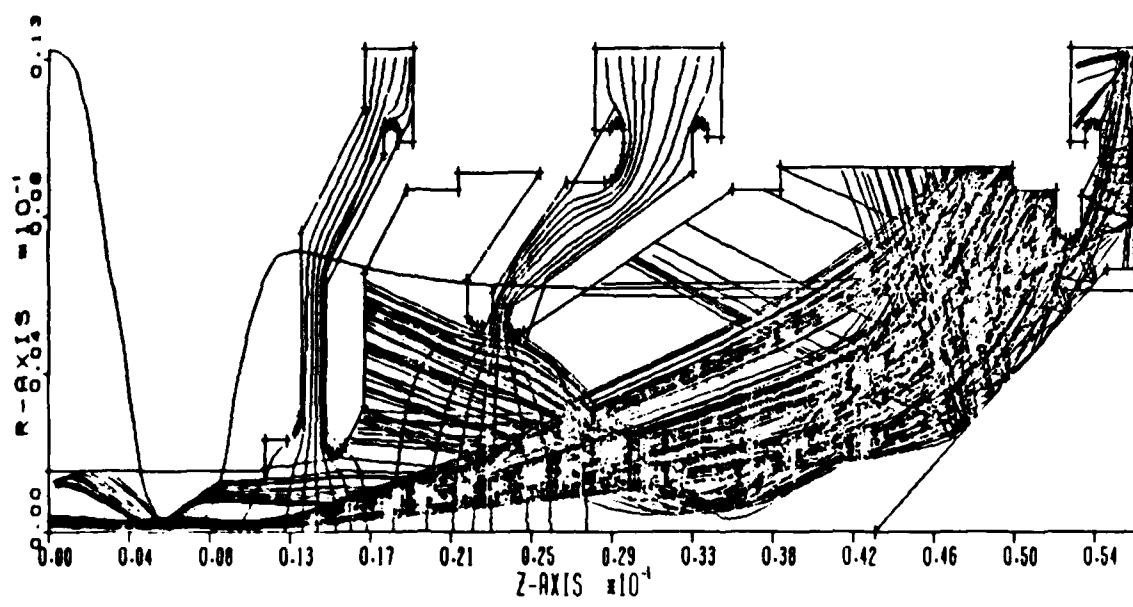
(c) E_b = 10,150 V, E_{b1} = 5180 V, E_{b2} = 2840 V, and E_s = 2000 V, all with respect to cathode.
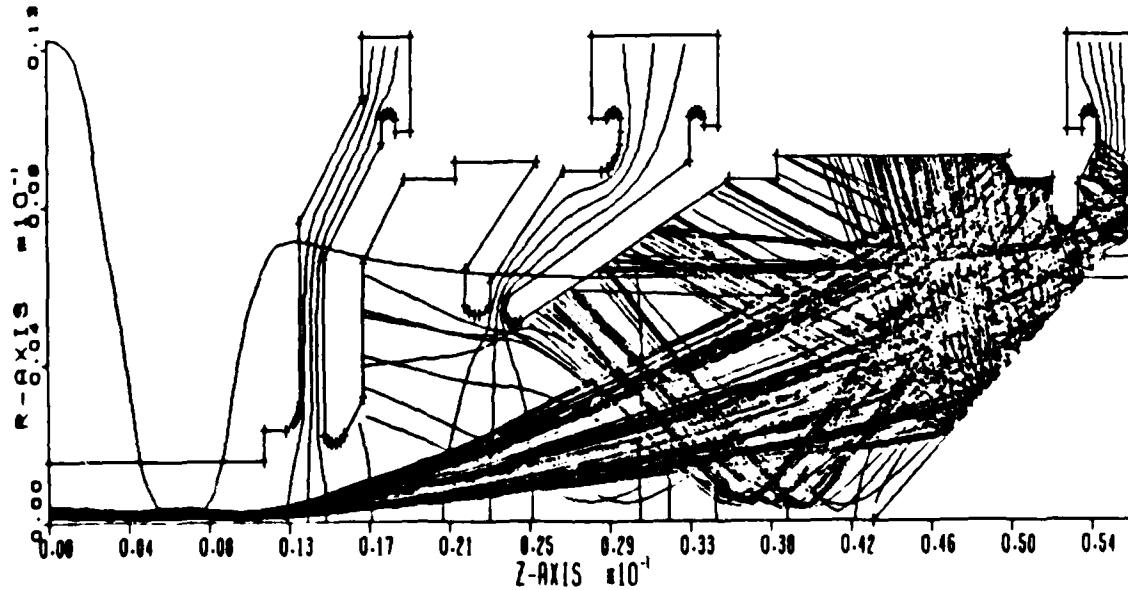
(d) E_b = 10, 150 V, E_{b1} = 5180 V, E_{b2} = 2840 V, and E_s = 2600 V, all with respect to cathode.
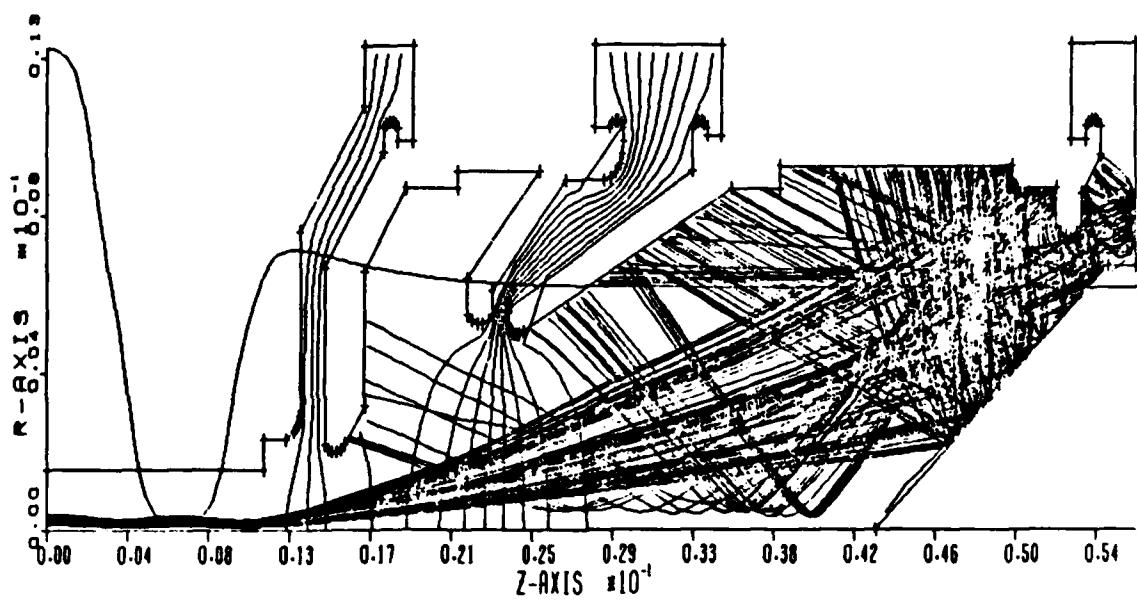
Fig. 23. Continued

(e) E_b = 10,150 V, E_{b1} = 5180 V, E_{b2} = 2840 V,
    and E_g = 2730 V, all with respect to cathode.
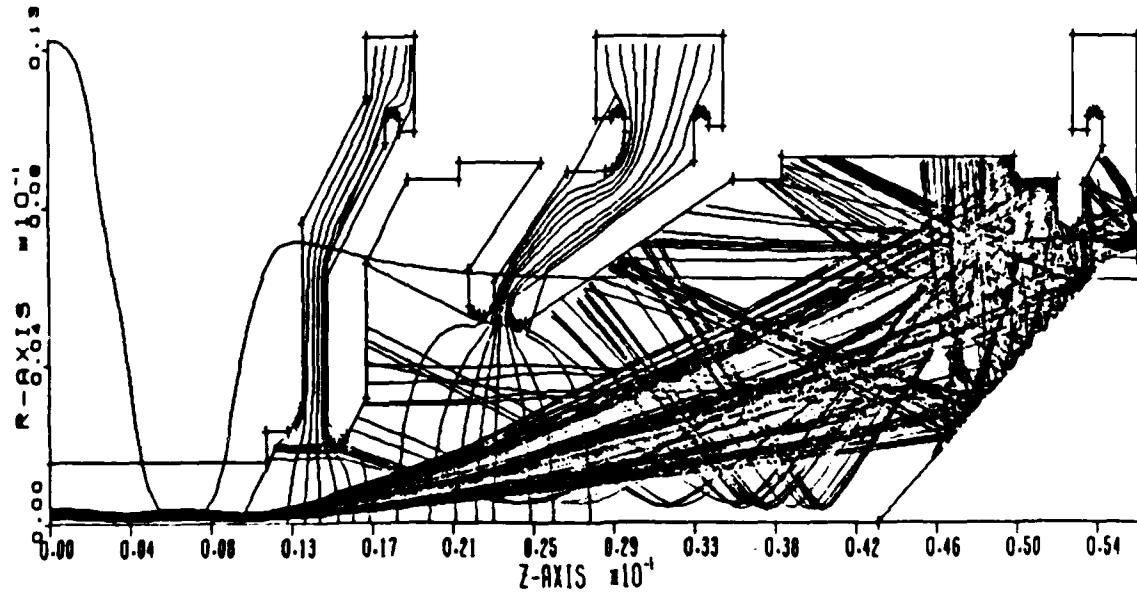
(f) E_b = 10,150 V, E_{b1} = 5180 V, E_{b2} = 2840 V,
    and E_g = 2790 V, all with respect to cathode.

Fig. 23. Continued

- 70 -
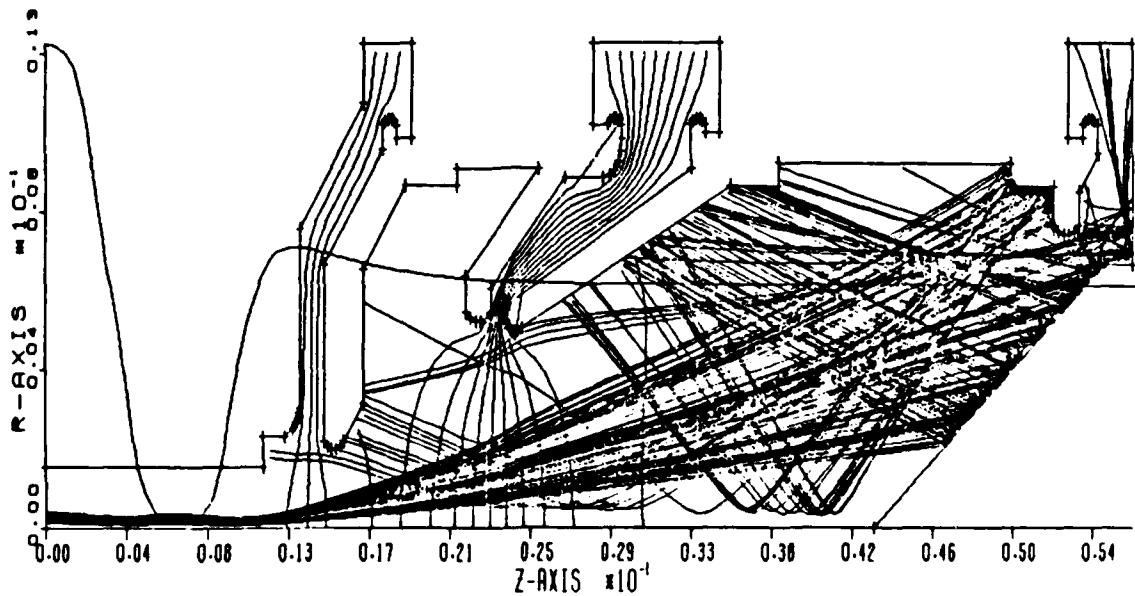
(g) $E_b = 10,150$ V, $E_{b1} = 5180$ V, $E_{b2} = 2840$ V, and $E_g = 2840$ V, all with respect to cathode.

Fig. 23. Continued

B. Single Bounce Secondary Model Performance with Varying Second Stage

A second set of curves was generated by holding the spike at 90 percent depression and varying the second stage depression from 50 to 70 percent. For continuity, both yield scaling factors of 0.7 and 1 were used. The resultant current distributions are shown in Fig. 24.

While both sets of curves exhibit a noticeable improvement in qualitative agreement to measured results over the entire energy range plotted, the most notable occurs for a yield scaling coefficient of 0.7 and when the body and first stage currents are treated collectively. For this case, the qualitative agreement between measured and predicted curves is very good for all cases except the spike.

While the error in the spike, body, and first stage currents is probably due to the omission of higher order secondary yields in our modeling, the higher overall current in the lesser depressed stages is most likely due to too large a yield scaling factor. This may be due to either of the two reasons previously mentioned.
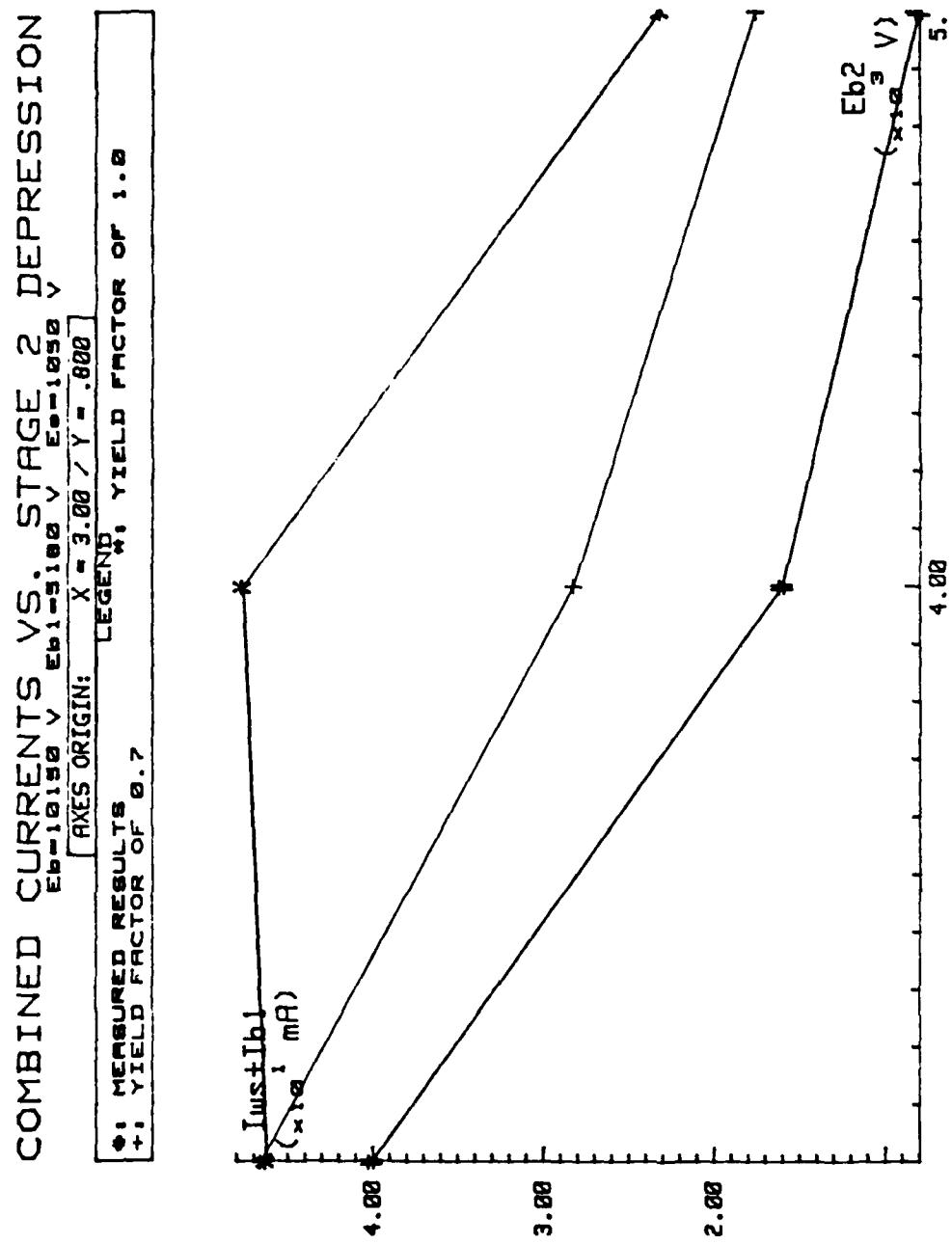
(a) Combined body and first stage current versus second stage depression.

Fig. 24. Measured and predicted electrode current collection curves versus second stage depression.

(b) Body current versus second stage depression.

Fig. 24. Continued

STAGE 1 CURRENT VS. STAGE 2 DEPRESSION
Eb=10150 V Eb1=5100 V Es=1050 V

AXES ORIGIN: X = 3.00 / Y = .300

LEGEND
*: MEASURED RESULTS   *: YIELD FACTOR OF 1.0
+: YIELD FACTOR OF 0.7

Ib1
(×10¹ mA)

3.00

2.00

1.00

4.00

Eb2
(×10³ V)

5.
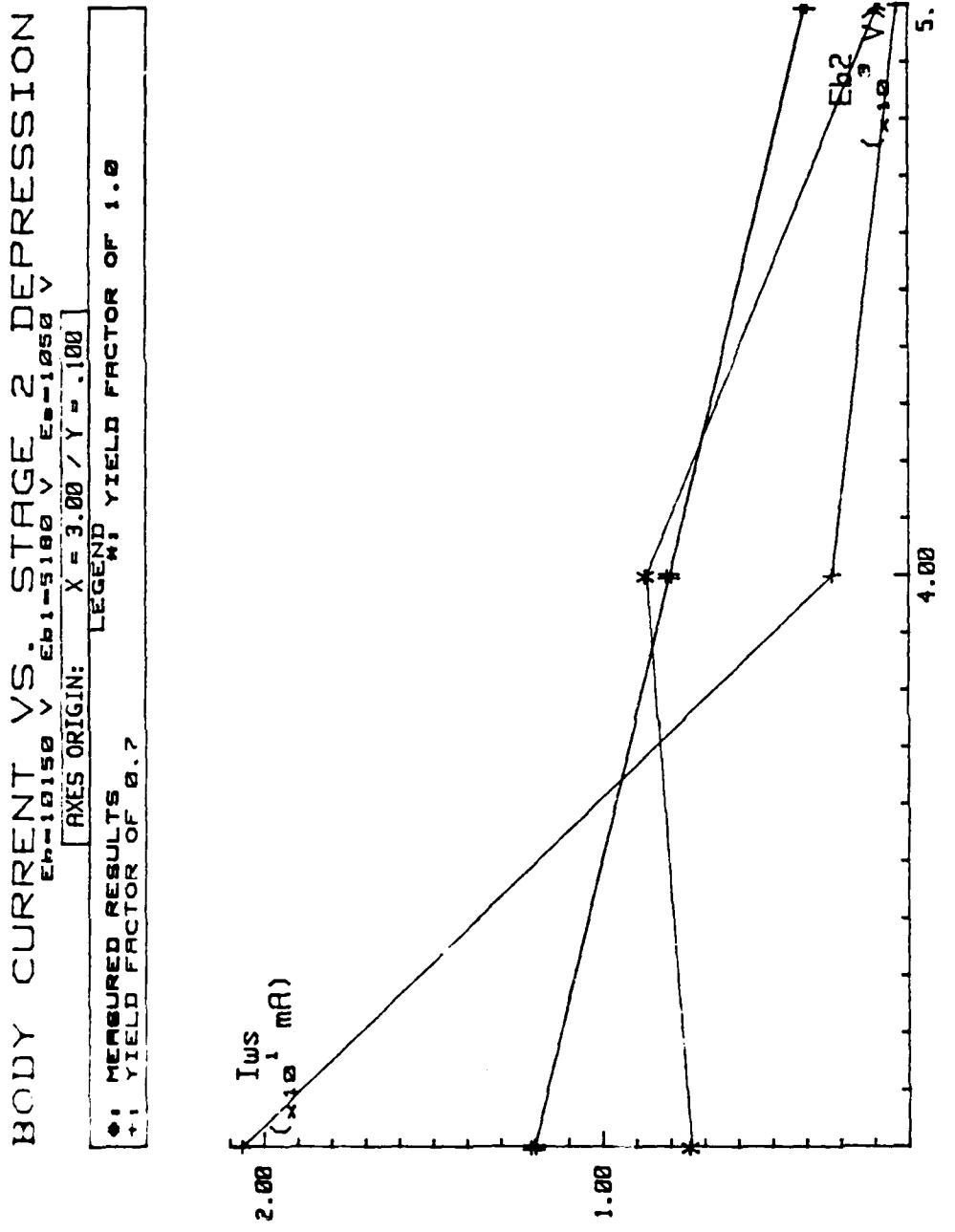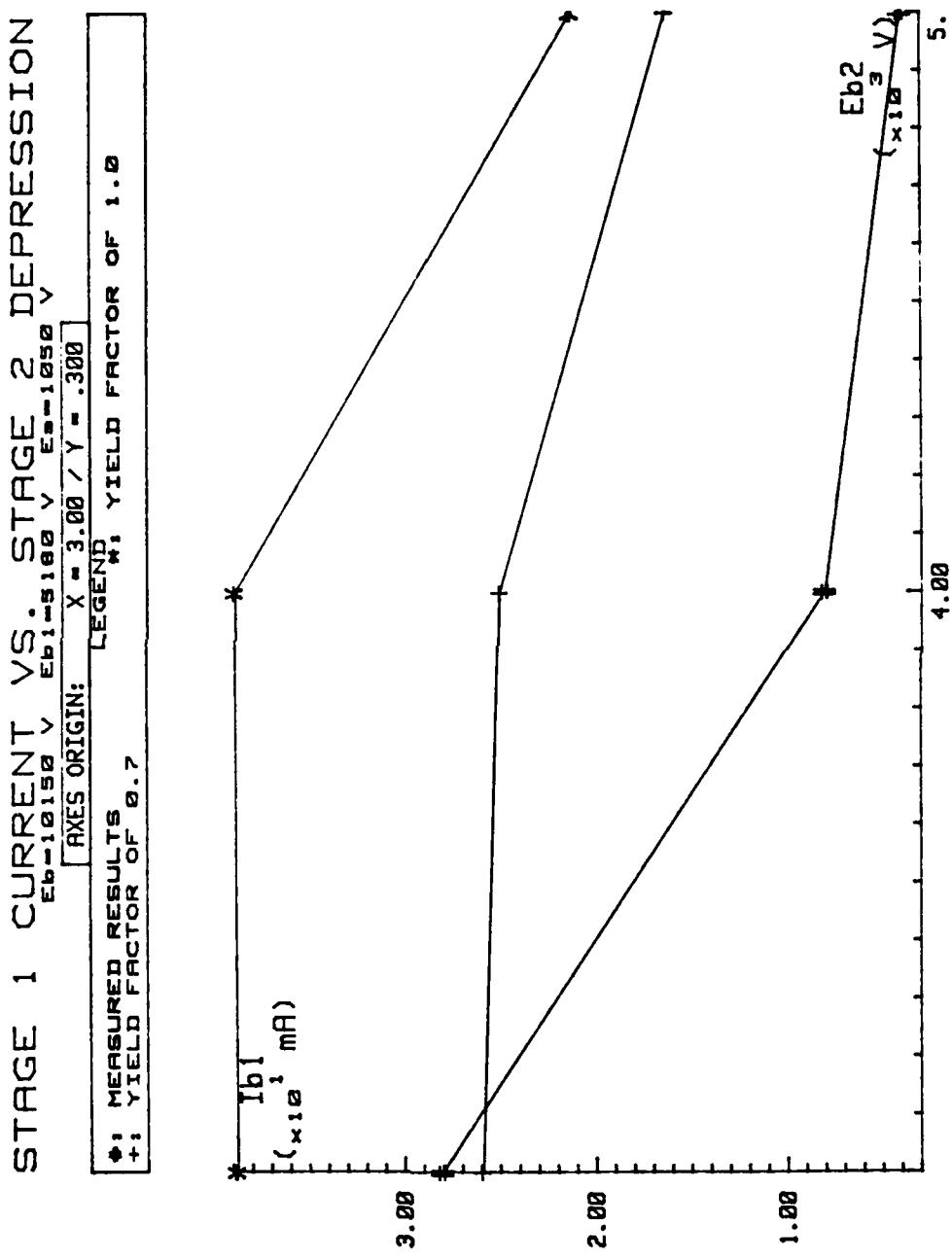
(c) First stage current versus second stage depression.

Fig. 24. Continued

- 75 -
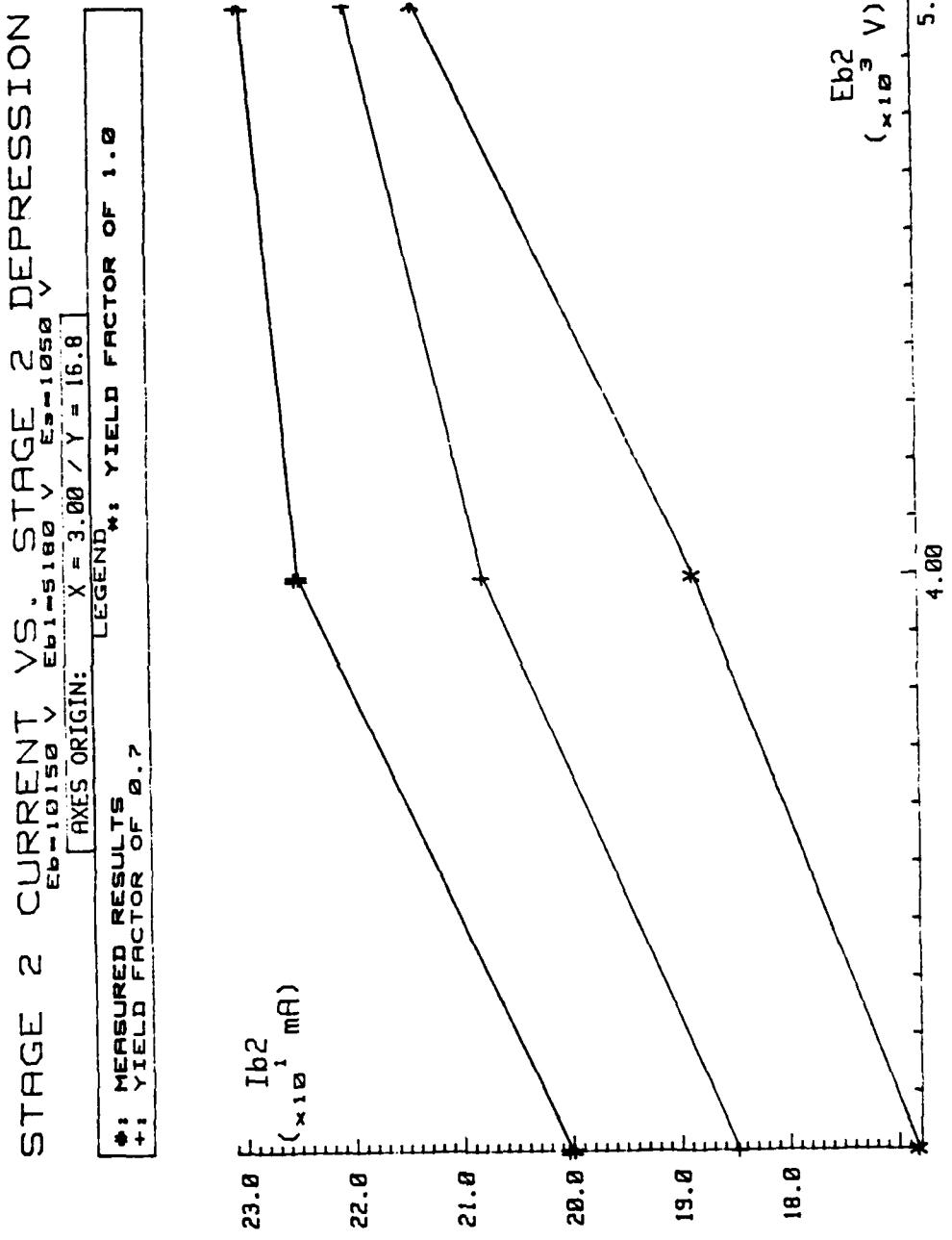
(d) Second stage current versus second stage depression.
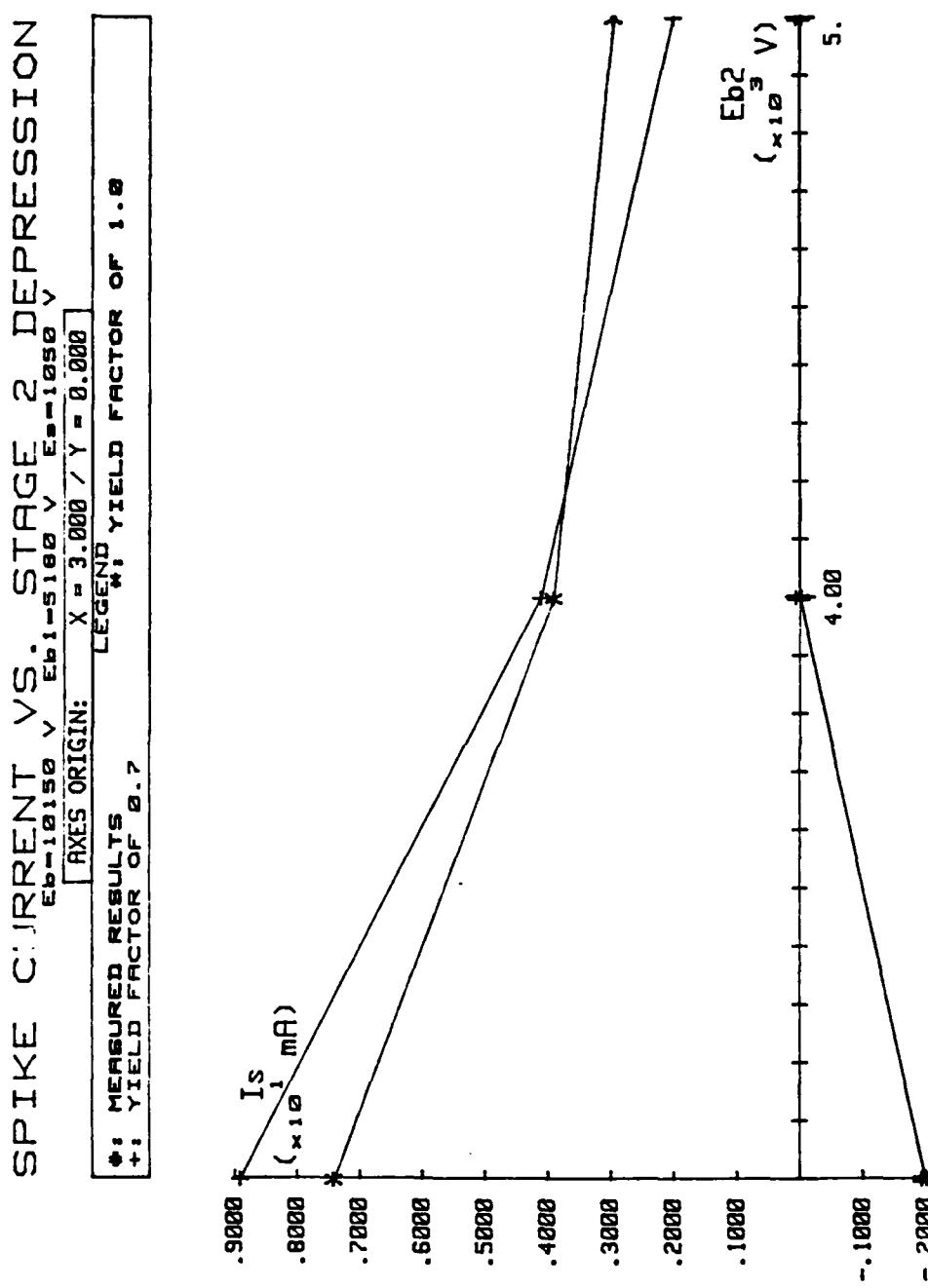
Fig. 24. Continued

(e) Spike current versus second stage depression.

Fig. 24. Continued

VI. CONCLUSIONS

Overall, the collector simulation suffered from the same major inaccuracy as the LRC simulations, namely, incorrect predictions of lesser depressed stages. The fact that the predictions exhibited some of the characteristic shapes of the measured curves would seemingly indicate that the model followed changes in primary initial conditions reasonably well.

The sources of error discussed earlier in the text are probably the areas in most need of improvement. At the time of this writing, the Raytheon Company is presently working on a model which employs a 3-ray representation for both the true as well as backscattered yield. Preliminary results are in better agreement to actual results than the 1-ray backscattered model employed in this thesis.

The problem of incorporating all higher order secondaries is workable, however, at great expense with today's computer technology. For situations in which only 1 species of secondaries is emitted, the model developed in this thesis is adequate. Out of all of the curves generated in this thesis, this condition would only apply to the first point of each of the curves in Fig. 20. Since these points happen to be in excellent agreement to the measured results anyway, there appears to be very little benefit in employing this option. The curves for which both fast and slow secondaries were emitted yielded much more appreciable error than secondaries only, and thus were omitted from the text of this thesis.

The final problem of surface texturing may be addressed by suitable application of the scaling factor. This, however, does not account for any preferential emission directions which may also be a consequence of the surface texture. Again, while this is being written, the Raytheon Company is presently undertaking the inclusion of an angular offset which may prove useful in optimizing model performance given a fixed material and surface texture. Until more work is reported in this area, however, these two features prove little more than an additional degree of freedom until experience dictates otherwise.

Finally, other areas of research which may be considered as well are the extension of these yield curves and distributions to any metal. Several possible methods of doing this have already been discussed.

Although much work still needs to be done on the model to achieve consistent quantitative agreement for all cases, the expense is "but a drop in the proverbial collector bucket" compared to savings in future MDC design.

REFERENCES

1. J. A. Dayton, Jr., H. G. Kosmahl, P. Ramins, and N. Stankiewicz, "Analytical Prediction and Experimental Verification of TWT and Depressed Collector Performance Using Multidimensional Computer Programs," IEEE Transactions on Electron Devices, Vol. ED-26, 1974, pp. 1589-1598.

2. J. A. Dayton, Jr., H. G. Kosmahl, P. Ramins, and N. Stankiewicz, "Analytical Prediction with Multidimensional Computer Programs and Experimental Verification of the Performance, at a Variety of Operating Conditions, of Two Traveling-Wave Tubes with Depressed Collectors," NASA Technical Paper No. 1449, 1979.

3. J. A. Dayton, Jr., H. G. Kosmahl, P. Ramins, and N. Stankiewicz, "Experimental Verification of a Computational Procedure for the Design of TWT-Refocuser-MDC Systems," IEEE Transactions on Electron Devices, Vol. ED-28, 1981, pp. 1480-1489.

4. J. A. Dayton, Jr., H. G. Kosmahl, P. Ramins, and N. Stankiewicz, "Analytical Prediction and Experimental Verification of Performance, at Various Operating Conditions, of a Dual-Mode Traveling-Wave Tube with Multistage Depressed Collectors," NASA Technical Paper No. 1831, 1981.

5. A. van der Ziel, Solid-State Physical Electronics, Prentice-Hall, Inc., Englewood Cliffs, New Jersey, 1961.

6. A. J. Dekker, Solid-State Physics, Prentice-Hall, Inc., Englewood Cliffs, New Jersey, 1957.

7. O. Hachenberg and W. Brauer, "Secondary Electron Emission from Solids," Advanced Electronics and Electron Physics, Vol. 11, 1959, pp. 413-499.

8. T. Koshikawa and R. Shimizu, "Secondary Electron and Backscattering Measurements for Polycrystalline Copper with a Spherical Retarding-Field Analyzer," Journal Physics D: Applied Physics, Vol. 6, 1973, pp. 1369-1380.

9. K. G. McKay, "Secondary Electron Emission," Advances in Electronics, Vol. 1, 1948, pp. 65-130.

10. J. L. H. Jonker, "The Angular Distribution of the Secondary Electrons of Nickel," Philips Research Report No. 6, 1951, pp. 372-387.

11. G. A. Harrower, "Energy Spectra of Secondary Electrons from Mo and W for Low Primary Energies," Phys. Review, Vol. 104, 1956, pp. 52-56.

12. H. O. Muller, "Die Abhangigkeit Der Sekundarelektronenemission Einiger Metalle Vom Einsallswinkel Des Primaren Kaathodenstrahls," Z. Physics, Vol. 104, 1937, pp. 475-486.

13. H. Bruining, "Secondary Electron Emission: Part II. Absorption of Secondary Electrons," Physica, Vol. 10, 1938, pp. 901-912.

14. A. N. Curren and T. A. Fox, "Traveling-Wave Tube Efficiency Improvement with Textured Pyrolytic Graphite Multistage Depressed Collector Electrodes," IEEE Electron Device Letters, Vol. EDL-2, 1981, pp. 252-254.

15. J. G. Trump and R. J. van de Graaff, "The Insulation of High Voltages in Vacuum," Journal of Applied Physics, Vol. 18, 1947, pp. 327-332.

16. R. Kollath, "Zur Energiezerteilung Der Sekundarelektronen," Ann. Physik, Vol. 1, 1947, pp. 357-380.

17. E. Rudberg, "Inelastic Scattering of Electrons from Solids," Phys. Review, Vol. 50, 1936, pp. 138-150.

18. A. Ralston and P. Rabinowitz, A First Course in Numerical Analysis, McGraw-Hill Book Company, New York, 1978.

19. J. E. Rowe, "A Large-Signal Analysis of the Traveling-Wave Amplifier: Theory and General Results," IEEE Transactions on Electron Devices, Vol. ED-3, 1956, pp. 39-57.

20. J. E. Rowe, Nonlinear Electron-Wave Interaction Phenomenon, Academic Press, Inc., New York, 1965.

21. N. J. Dionne and H.-J. Krahn, "Three-Dimensional Gun Program," Final Report No. PT-5599, Raytheon Company, Microwave and Power Tube Division, Waltham, Massachusetts, June 12, 1980.

22. R. Forman, "Secondary-Electron-Emission Properties of Conducting Surfaces with Application to Multistage Depressed Collectors for Microwave Amplifiers," NASA Technical Paper No. 1097, 1977.

APPENDIX A

DERIVATION OF PLANAR CURRENT EXPRESSION

Since the purpose of this derivation is to eventually have an expression for the planar current in the y-z plane, it is necessary to find expressions relating the initial current weighting vector, $\vec{V}_1$, to the y and z component vectors, $\vec{V}_2$ and $\vec{V}_3$, respectively. These vectors are shown in Fig. A.1 for an arbitrary direction defined by the angles θ and ϕ.

The vector $\vec{V}_1$ may be broken up into components as

$$\vec{V}_1 = \vec{V}_3 + \vec{V}_4 = |\vec{V}_3| \, \hat{z} + \vec{V}_4 \qquad (A.1)$$

Vector $\vec{V}_4$ may also be written as the sum of its component vectors,

$$\vec{V}_4 = \vec{V}_2 + \vec{V}_5 = |\vec{V}_2| \, \hat{y} + |\vec{V}_5| \, \hat{x} \qquad (A.2)$$

Also, $|\vec{V}_3|$ and $|\vec{V}_4|$ may be related to $|\vec{V}_1|$ by the relations

$$|\vec{V}_4| = |\vec{V}_1| \, \sin(\theta) \qquad (A.3)$$

and

$$|\vec{V}_3| = |\vec{V}_1| \, \cos(\theta) \qquad (A.4)$$

- 82 -
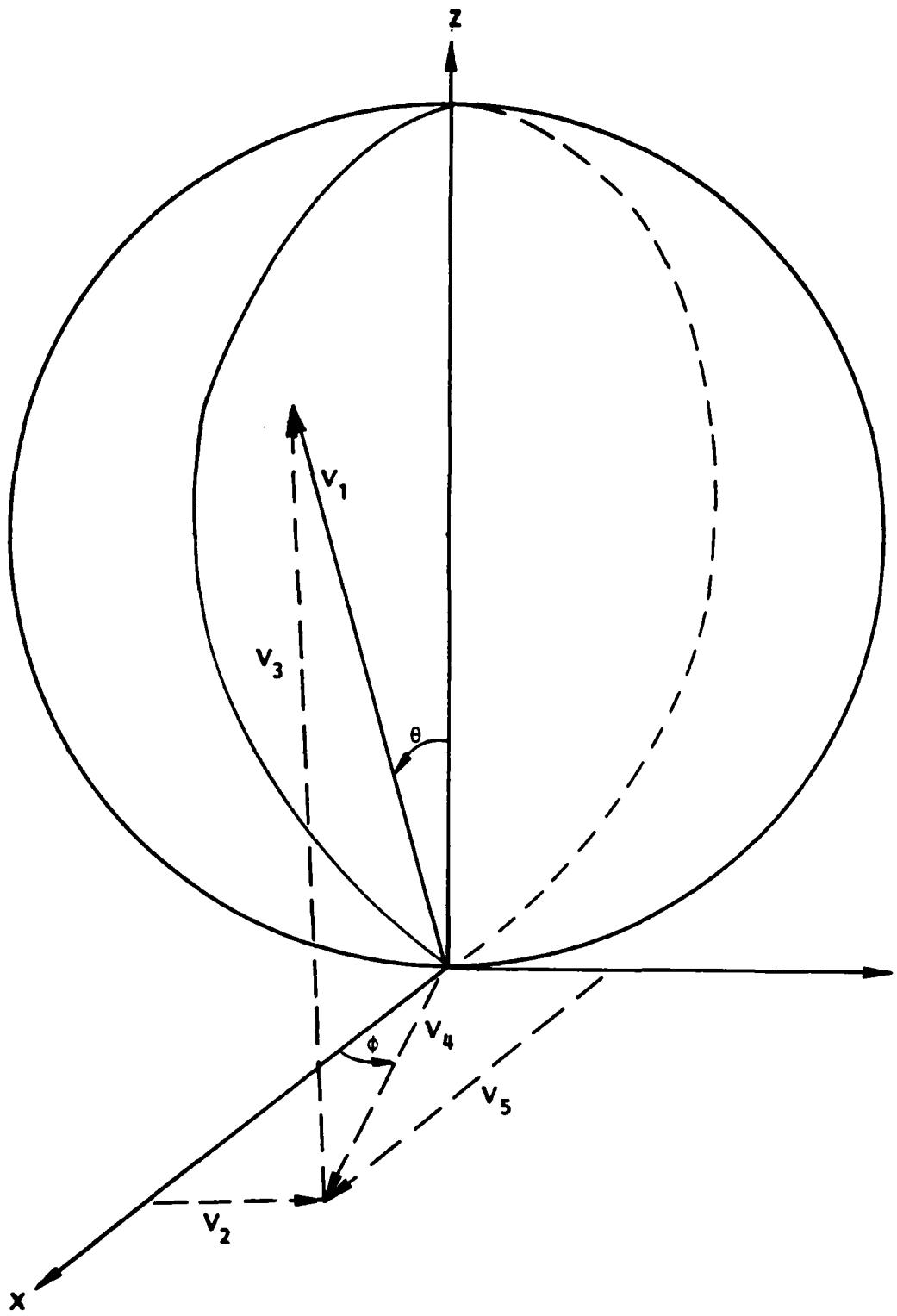
Fig. A.1. Three-dimensional slow secondary distribution
projections on a two-dimensional plane.

- 83 -

Similarly, the magnitudes of $\vec{V}_2$ and $\vec{V}_5$ may be related to $|\vec{V}_4|$ as

$$|\vec{V}_2| = |\vec{V}_4| \, \sin(\phi) \qquad (A.5)$$

and

$$|\vec{V}_5| = |\vec{V}_4| \, \cos(\phi) \qquad (A.6)$$

Substituting Eq. A.4 into Eq. A.1 gives

$$\vec{V}_1 = |\vec{V}_1| \, \cos(\theta) \, \hat{z} + \vec{V}_4 \qquad (A.7)$$

Now, using Eqs. A.2, A.3, A.5, and A.6, Eq. A.7 may be written as

$$\vec{V}_1 = |\vec{V}_1| \, \cos(\theta) \, \hat{z} + |\vec{V}_1| \, \sin(\theta) \, \sin(\phi) \, \hat{y} + |\vec{V}_1| \, \sin(\theta) \, \cos(\phi) \, \hat{x} \qquad (A.8)$$

Breaking $\vec{V}_1$ up into components, with one component directed in the $\hat{x}$ direction and one component normal to that direction (y-z plane), we may write

$$V_1 = V_{1x} \, \hat{x} + V_{1\perp} \, \hat{\perp} \qquad (A.9)$$

Equation A.18 may now be put into the form of Eq. A.9 by defining

$$V_{1\perp} \equiv |V_1| \left(\cos^2(\theta) + \sin^2(\theta) \, \sin^2(\phi) \right)^{1/2} \qquad (A.10)$$

- 84 -

and

$$\hat{1} \equiv \left|\vec{V}_1\right| \left(\sin(\theta) \sin(\phi) \hat{y} + \cos(\theta) \hat{z}\right)/V_{1\perp} \qquad (A.11)$$

By definition, $\left|\vec{V}_1\right|$ is just the distribution function, which describes the number of electrons emitted per unit time per solid angle.

As mentioned previously, this distribution function takes the form of

$$\left|\vec{V}_1\right| = Jo \cos(\theta) \qquad (A.12)$$

From Eqs. A.10 and A.12, we see that the magnitude of the total number of emitted electrons per unit area per unit time projected on the y-z plane is simply

$$V_{1\perp} = Jo \cos(\theta) \left(\cos^2(\theta) + \sin^2(\theta) \sin^2(\phi)\right)^{1/2} \qquad (A.13)$$

Thus, the total number of electrons emitted per unit time in the y-z plane may be determined by multiplying $V_{1\perp}$ by the solid angle and integrating over a specified region defined by θ and ϕ. The unit solid angle may now be written as

$$d? = \sin(\theta) \, d\theta \, d\phi \qquad (A.14)$$

An expression for the differential planar current emitted for a given direction may now be written as

- 85 -

$$dJ_{y-z} = Jo \cos(\theta) \left(\cos^2(\theta) + \sin^2(\theta) \sin^2(\phi)\right)^{1/2} \sin(\theta) \, d\theta \, d\phi \quad (A.15)$$

Due to symmetry, integration need only be performed over the hemisphere defined by x-z plane. An expression for the total planar current contained between the two angles, θ_1 and θ_2, may now be derived from Eq. A.15 as

$$\int dJ_{y-z} = Jo \int_{\theta_1}^{\theta_2} \cos(\theta) \sin(\theta) \int_0^\pi \left(\cos^2(\theta) + \sin^2(\theta) \sin^2(\phi)\right)^{1/2} d\phi \, d\theta$$

$$(A.16)$$

since

$$\sin^2(x) = 1 - \cos^2(x) \quad (A.17)$$

Eq. A.16 may be written as

$$\int dJ_{y-z} = Jo \int_{\theta_1}^{\theta_2} \cos(\theta) \sin(\theta) \int_0^\pi \left(\cos^2(\theta) + \sin^2(\theta)(1 - \cos^2(\phi))\right)^{1/2} d\phi \, d\theta$$

$$(A.18)$$

which may also be written as

$$\int dJ_{y-z} = Jo \int_{\theta_1}^{\theta_2} \cos(\theta) \sin(\theta) \int_0^\pi \left(1 - \sin^2(\theta) \cos^2(\phi)\right)^{1/2} d\phi \, d\theta \quad (A.19)$$

Defining

- 86 -

$$\phi \equiv \pi/2 - \nu \qquad (A.20)$$

we see that

$$d\phi = -d\nu \qquad (A.21)$$

and noting that the limits also change, Eq. A.19 may now be written as

$$\int dJ_{y-z} = -Jo \int_{\theta_1}^{\theta_2} \cos(\theta) \sin(\theta) \int_{\pi/2}^{-\pi/2} \left(1 - \sin^2(\theta) \cos^2(\pi/2 - \nu)\right)^{1/2} d\nu \, d\theta$$

$$(A.22)$$

Since

$$\cos(\pi/2 - x) = \sin(x) \qquad (A.23)$$

Eq. A.22 becomes

$$\int dJ_{y-z} = J1 \int_{\theta_1}^{\theta_2} \cos(\theta) \sin(\theta) \int_{-\pi/2}^{\pi/2} \left(1 - \sin^2(\theta) \sin^2(\gamma)\right)^{1/2} d\nu \, d\theta$$

$$(A.24)$$

The integral on ν may be evaluated by noting that

$$\eta \left(1 - a^2 \sin^2(\nu)\right)^{1/2} d\nu = E(\nu, a)$$

Equation A.24 may be written as
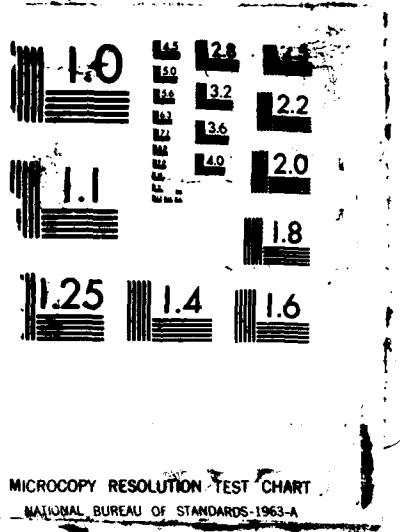
MICROCOPY RESOLUTION TEST CHART

NATIONAL BUREAU OF STANDARDS-1963-A

$$\int dJ_{y-z} = Jo \int_{\theta_1}^{\theta_2} \cos(\theta) \sin(\theta) \left. E(\nu, \sin(\theta)) \right|_{\nu = -\pi/2}^{\nu = \pi/2} d\theta \quad (A.26)$$

Evaluating the term inside the integral, Eq. A.26 becomes

$$\int dJ_{y-z} = Jo \int_{\theta_1}^{\theta_2} \cos(\theta) \sin(\theta) \left\{ E(\pi/2, \sin(\theta)) - E(-\pi/2, \sin(\theta)) \right\} d\theta$$

$$(A.27)$$

It can also be shown that $E(-\nu, k) = -E(\nu, k)$, so Eq. A.27 may be written as

$$\int dJ_{y-z} = Jo \int_{\theta_1}^{\theta_2} \cos(\theta) \sin(\theta) \left\{ E(\pi/2, \sin(\theta)) + E(\pi/2, \sin(\theta)) \right\}$$

$$= 2Jo \int_{\theta_1}^{\theta_2} \cos(\theta) \sin(\theta) E(\pi/2, \sin(\theta)) d\theta \quad . \quad (A.28)$$

Noting that $E(\pi/2, k)$ is also a special case of $E(\nu, k)$, we will define the special case as $\widetilde{E}(k)$ and also note the relation that

$$E(k) = \pi/2 \left[1 - 2^2 k^2 - \frac{1^2 \cdot 3}{2^2 \cdot 4^2} k^4 - \ldots - \left\{ \frac{(2n - 1)!!}{2^n \, n!} \right\}^2 \frac{k^{2n}}{(2n - 1)} - \ldots \right]$$

$$(A.29)$$

Using this fact, Eq. A.28 may be rewritten as

$$\int dJ_{y-z} = \pi Jo \int_{\theta_1}^{\theta_2} \cos(\theta) \sin(\theta) \left[1 - \sum_{n=1}^{\infty} \left\{ \frac{(2n - 1)!!}{2^n \, n!} \right\}^2 \frac{k^{2n}}{(2n - 1)} \right] d\theta$$

$$(A.30)$$

Since the integral of the sum is the sum of the integrals, Eq. A.30 may be rewritten as

$$\int dJ_{y-z} = \pi Jo \left\{ \int_{\theta_1}^{\theta_2} \cos(\theta) \sin(\theta) d\theta \right.$$

$$\left. - \sum_{n=1}^{\infty} \left\{ \frac{(2n-1)!!}{2^n n!} \right\}^2 \frac{1}{(2n-1)} \int_{\theta_1}^{\theta_2} \cos(\theta) \sin^{2n+1}(\theta) d\theta \right\} \qquad (A.31)$$

In general,

$$\int \cos(\theta) \sin(\theta) d\theta = \frac{1}{m+1} \sin^{m+1}(\theta) \qquad (A.32)$$

So, substituting Eq. A.32 into Eq. A.31, we get an expression for the projected planar current emitted from the region defined by θ_1 and θ_2 as

$$J_{y-z} = \pi Jo \left\{ 1/2 \; \sin^2(\theta_2) - \sin^2(\theta_1) \right.$$

$$\left. - \sum_{n=1}^{\infty} \left\{ \frac{(2n-3)!!}{2^n n!} \right\}^2 \frac{(2n-1)}{2(n+1)} \left(\sin^{2(n+1)}(\theta_2) - \sin^{2(n+1)}(\theta_1) \right) \right\} (A.33)$$

Equation A.33 may now be solved using numerical procedures.

- 89 -

APPENDIX B

PROOF OF RATES OF INCREASE WITH INCIDENT ANGLE

Definitions

$I(E_p, \theta_i)$ is the current of the primary beam with energy E_p and making an angle of θ_i with respect to the surface normal

$Y(E_p, \theta_i)$ is the total secondary yield for the primary current $I(E_p, \theta_i)$

$B(E_p, \theta_i)$ is the backscattered yield for the primary current $I(E_p, \theta_i)$

$S(E_p, \theta_i)$ is the true secondary yield for the primary current $I(E_p, \theta_i)$

$y(E_p, \theta_i)$ is the total yield coefficient for the primary current $I(E_p, \theta_i)$

$b(E_p, \theta_i)$ is the backscattering coefficient for the primary current $I(E_p, \theta_i)$

with θ_i shown in Fig. B.1 as being the angle of incidence with respect to the surface normal.

For brevity, define a general function of the form $f(E_b, \theta_i)$ to be $f_{E_b}\theta_i$. Now for normal incidence by definition,

$$B_{E_p}0 = I_{E_p}0 \, b_{E_p}0 \qquad (B.1)$$

also
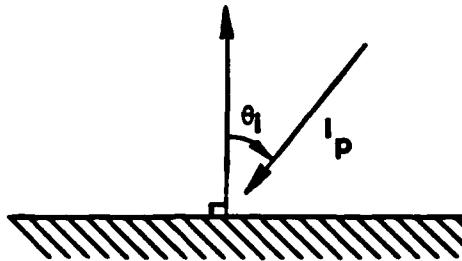
Fig. B.1. Definition of incident angle as used in this appendix
and everywhere in the rest of this report.

$$Y_{E_p0} = I_{E_p0} \, y_{E_p0} \qquad\qquad (B.2)$$

and

$$S_{E_p0} = I_{E_p0} \left(y_{E_p0} - b_{E_p0} \right) \qquad\qquad (B.3)$$

for a beam with incidence of 67 degrees, we have

$$B_{E_p67} = I_{E_p67} \, b_{E_p67} \qquad\qquad (B.4)$$

also,

$$Y_{E_p67} = I_{E_p67} \, b_{E_p67} \, , \qquad\qquad (B.5)$$

and

$$S_{E_p}67\left(^yE_p67 - {^b}_{E_p}67\right) \qquad\qquad (B.6)$$

Defining the percent increase of a functional value with angle as the ratio of the functional value at the largest angle to the functional value at normal incidence, we may write the percent increase in true secondary yield, F^S, as

$$F^S \equiv \frac{S_{E_p}67}{S_{E_p}0} = \frac{I_{E_p}67\left(^yE_p67 - {^b}_{E_p}67\right)}{I_{E_p}0\left(^yE_p0 - {^b}_{E_p}0\right)} \qquad\qquad (B.7)$$

and the percent increase in backscattered yield, F^b, as

$$F^B = \frac{B_{E_p}67}{B_{E_o}0} = \frac{I_{E_p}67\ {^b}_{E_p}67}{I_{E_p}0\ {^b}_{e_p}0} \qquad\qquad (B.8)$$

Now, in order to ensure that the only change in yields is that due to the angular dependence, let

$$I_{E_p}67 = I_{E_p}0 \qquad\qquad (B.9)$$

With the above relation, Eqs. b.7 and B.8 become, respectively,

$$F^S = \frac{\left(^yE_p67 - {^b}_{E_p}67\right)}{\left(^yE_p0 - {^b}_{E_p}0\right)} \qquad\qquad (B.10)$$

and

$$F^B = \frac{{^b}_{E_p}67}{{^b}_{E_p}0} \qquad\qquad (B.11)$$

Defining

$$F^y = \frac{y_{E_p}67}{y_{E_p}0} \tag{B.12}$$

we may rewrite Eq. B.10 as

$$F^S = \frac{\left(F^y\, y_{E_p}0 - F^B\, b_{E_p}0\right)}{\left(y_{E_p}0 - b_{E_p}0\right)} = \frac{\left(F^B\left\{\frac{F^y}{F^B}\right\}y_{E_p}0 - b_{E_p}0\right)}{\left(y_{E_p}0 - b_{E_p}0\right)} \tag{B.13}$$

Now, it is evident that if

$$\frac{\left(\left\{\frac{F^y}{F^B}\right\}y_{E_p}0 - b_{E_p}0\right)}{y_{E_p}0 - b_{E_p}0} \begin{array}{c} < 1 \\ = 1 \\ > 1 \end{array} \quad \text{then,} \quad \begin{array}{c} F^S < F^B \\ F^S = F^B \\ F^S > F^B \end{array} \tag{B.14}$$

By definition,

$$y_{E_p\theta_1} > b_{E_p\theta_1} \tag{B.15}$$

Additionally, for all cases tabulated in Table 2,

$$F^y > F^B \tag{B.16}$$

Relation of Eq. B.16 implies that

$$\frac{F^y}{F^B} > 1 \qquad \cdot \tag{B.17}$$

which in turn implies that

$$\left\{ \frac{F^y}{F^B} \right\} y_{E_p0} > y_{E_p0} \qquad\qquad \text{(B.18)}$$

or

$$\left\{ \frac{F^B}{F^y} \right\} y_{E_p0} = y_{E_p0} - b_{E_p0} \qquad\qquad \text{(B.19)}$$

or that

$$\frac{\left(\left\{ \frac{F^y}{F^B} \right\} y_{E_p0} - b_{E_p0} \right)}{\left(y_{E_p0} - b_{E_p0} \right)} > 1 \qquad\qquad \text{(B.20)}$$

From Eq. B.14, it can thus be shown that

$$F^S > F^B \qquad\qquad \text{(B.21)}$$